

Reconfigurable Intelligent Surface Aided TeraHertz Communications Under Misalignment and Hardware Impairments

Hongyang Du, Jiayi Zhang, *Senior Member, IEEE*, Ke Guan, *Senior Member, IEEE*,
Bo Ai, *Senior Member, IEEE*, and Thomas Kürner, *Fellow, IEEE*

Abstract

TeraHertz (THz) communications are envisioned to help satisfy the ever high data rates demand with massive bandwidth in the future wireless communication systems. However, severe path attenuation, transceiver antenna misalignment, and hardware imperfection greatly alleviate the performance of THz communications. To solve this challenge, we utilize the recently proposed reconfigurable intelligent surface (RIS) technology and provide a comprehensive analytical framework of RIS-aided THz communications. More specifically, we first prove that the small-scale amplitude fading of THz signals can be exactly modeled by the fluctuating two-ray distribution based on recent measurements. Exact statistical characterizations of end-to-end signal-to-noise plus distortion ratio (SNDR) and signal-to-noise ratio (SNR) are derived. Moreover, we propose a novel method of optimizing the phase-shifts at the RIS elements under discrete phase constraints. Finally, we derive analytical expressions for the outage probability and ergodic capacity, respectively. The tight upper bounds of ergodic capacity for both ideal and non-ideal radio frequency chains are obtained. We provided Monte-Carlo simulations to validate the accuracy of our results. It is interesting to find that the impact of path loss is more pronounced compared to others, and increasing the number of elements at the RIS can significantly improve the THz communication system performance.

Index Terms

Fluctuating two-ray, phase-shifts, reconfigurable intelligent surface, THz communications.

H. Du and J. Zhang are with the School of Electronic and Information Engineering, Beijing Jiaotong University, Beijing 100044, China. (e-mail: {17211140; jiayizhang}@bjtu.edu.cn)

K. Guan and B. Ai are with the State Key Laboratory of Rail Traffic Control and Safety, Beijing Jiaotong University, Beijing 100044, China. (e-mail: {boai; kguan}@bjtu.edu.cn)

T. Kürner is with Institute for Communications Technology (IfN), Technische Universität Braunschweig, 38106 Brunswick, Germany. (e-mail: kuerner@ifn.ing.tu-bs.de)

I. INTRODUCTION

In the past few years, wireless data traffic has been witnessing unprecedented expansion. Several technological advances, such as artificial intelligence, massive multiple-input multiple-output (MIMO) systems, and full-duplexing, have been presented [1] while the wireless world moves towards the sixth generation (6G). However, developing new spectrum resources for future 6G communication systems is urgently demanded.

Because of the high spectrum availability, THz communication emerges as a key candidate in future generations [2], [3]. However, THz signals have considerably high sensitivity to blockage, i.e., in urban environments with high obstacle density. Thus, the direct usage of THz-band in wireless access scenarios is very challenging. Recently, the reconfigurable intelligent surface (RIS) technology has drawn increasing attention [4]–[6] due to its ability to improve both spectrum and energy efficiency in a cost-effective way. A RIS can be easily coated on existing infrastructures such as walls of buildings, facilitating low-cost and low-complexity implementation. By smartly adjusting the scattering properties of its reflecting elements, the RIS can form equally strong beams in any direction for THz signals.

However, how to model the small-scale amplitude fading of THz signals is still an open question. Methods of modeling and evaluating the performance of THz communications have been extensively studied in the literature. In particular, the authors in [7] delivered a simplified molecular absorption loss model that was used in [8] for the quantification of the THz link capacity. However, the THz system performance is overestimated by neglecting small-scale fading. In [9], the envelope of the fading coefficient was proved by the authors experimentally to follow the Nakagami- m distribution under both non-line-of-sight (NLoS) and line-of-sight (LoS) conditions. Similarly, experimental verifications of the existence of shadowing in the 300 GHz band were exploited in [10]. Very recently, a THz measurement campaign was conducted in a train test center with trains, tracks, and lampposts [11], which is highly similar to typical train-to-train scenarios. On the other hand, the fluctuating two-ray (FTR) fading model [12] is a generalization of the two-wave with diffuse power fading model, which allows the constant amplitude specular waves of LoS propagation to fluctuate randomly. We fit the measurement data to a Gaussian, Rician, Nakagami- m and FTR distributions, respectively, and prove that the FTR distribution performs a much better fit than others.

Therefore, with the help of the FTR fading model, we propose a comprehensive analytical framework for RIS-aided THz communications. The impact of transceivers antenna gains, the level of transceivers

hardware imperfections, the transmission distance, the misalignment between the RIS and the destination, the operation frequency, and the environmental conditions including temperature, humidity, and pressure, are all considered in our framework. The main contributions of this paper are summarized as follows:

- In order to model the small-scale amplitude fading of THz signals, we prove that the FTR distribution performs a much better fit than other fading models with the help of the THz measurement data [11]. We derive exact probability density function (PDF) and cumulative distribution function (CDF) expressions of end-to-end signal-to-noise ratio (SNR) and signal-to-noise plus distortion ratio (SNDR) in terms of the multivariate Fox's H -function, respectively.
- For the practical RIS with a finite number of phase-shifts at each element, we propose a binary search tree based phase optimization method. The impact of different number of discrete phase-shifts levels is revealed, and we find that using large discrete phase-shifts levels is able to achieve the performance of RIS with continuous phase-shifts.
- We derive novel exact closed-form expressions of outage probability (OP) and ergodic capacity for the RIS-aided THz communication system with ideal radio frequency (RF) chains. Moreover, the tight upper bound expressions of ergodic capacity for both ideal and non-ideal RF chains are obtained. Important physical and engineering insights have been revealed from the derived results.

The remainder of the paper is structured as follows. We briefly introduce the RIS-aided THz communication system model in Section II. Section III presents the optimal phase-shifts of the RIS's reflector array under discrete levels constraints. In Section IV, we derive exact PDF and CDF expressions of end-to-end SNR and SNDR of the considered system. Important performance metrics, such as OP and ergodic capacity, are obtained in Section V. Numerical results accompanied with Monte-Carlo simulations are presented in Section VI. Finally, the main conclusions are drawn in Section VII.

II. SYSTEM AND SIGNAL MODEL

A. System Description

We focus on a single cell of THz communications with blockages in the propagation environment. As shown in Fig. 1, the transmitted signal from S is often blocked by obstacles. Thus, we assume that the direct link between S and D is weak enough to be ignored. This assumption is likely to be true for THz communication systems that are known to suffer from high path and penetration losses resulting in signal blockages. In this case, an RIS equipped with L reflecting elements is set up between the S \rightarrow D link to

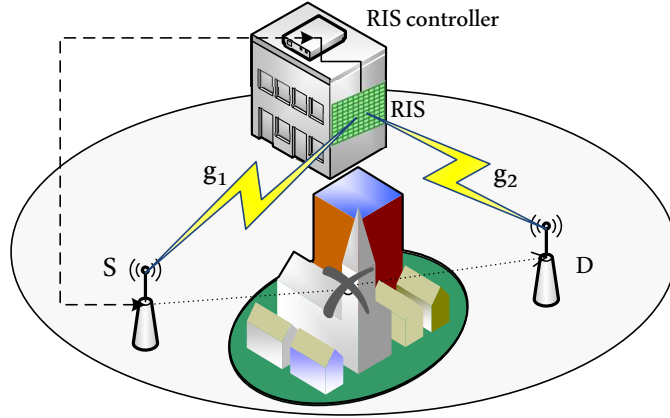


Fig. 1. System model of RIS-aided THz communication system.

assist the communications. Both the source (S) and destination (D) are assumed to be equipped with one antenna¹. Moreover, the controller coordinates S and RIS for channel acquisition and data transmission [14].

The signal received from S through RIS for D can be expressed as

$$y = h_L h_P \mathbf{g}_1 \Phi \mathbf{g}_2 x + n, \quad (1)$$

where h_L is the path gain, h_P denotes the misalignment fading that results in pointing errors, and $\mathbf{g}_1 \in C^{1 \times L}$ denotes the small-scale fading between S and RIS. $\Phi = \beta \text{diag} [e^{i\phi_1}, \dots, e^{i\phi_L}]$ with $\beta \in (0, 1]$ is the phase-shifts matrix², where ϕ_ℓ denotes the phase-shift of the ℓ th reflecting element of the RIS and $i = \sqrt{-1}$, $\mathbf{g}_2 \in C^{L \times 1}$ denotes the small-scale fading between the RIS and the D, n is modeled as a complex zero-mean additive white Gaussian process with variance N_0 , x is transmit signal satisfying $\mathbb{E} [|x|^2] = P$ and P is the transmit power.

Herein, we consider a practical THz communication system. First, the received signal model given in (1) neglects the effect of physical RF transceivers imperfections that is detrimental in high data rate systems [15], [16], including in-phase and quadrature imbalance (IQI), phase noise (PHN), and amplifier non-linearities. Furthermore, the phase-shift at each element of the RIS can only take a finite number of discrete values due to the hardware constraints.

¹Notice that our analysis can be generalized to the case of multiple-antennas BS or user. This is due to the reason that we prove that the FTR distribution performs a much better fit to the small-scale amplitude fading of THz communications than other fading models in Section II-B, and the single FTR distribution can be regarded as the approximation to the distribution of the sum of FTR RVs [13]. Thus, when the BS or user is equipped with multiple-antennas, we can still use the single FTR distribution to model the RIS-aided THz communications with the help of the accurate approximation method proposed in [13]. Furthermore, the signal in THz communications is highly directional, which implies that the interference among THz links can be significantly small. Therefore, the interference from other cell-users is ignored.

²In practice, each element of the RIS is usually designed to maximize the signal reflection β . However, the value of β does not affect the algorithm design. Without loss of generality, we set $\beta = 1$ for simplicity.

These imperfections result in a mismatch between what is actually emitted and the transmit signal x . Furthermore, the received signal is distorted during the reception processing. More specifically, IQI will cause the mirror-interference, local oscillator PHN will result to adjacent carrier interference, and amplifiers non-linearities can be modeled as a complex Gaussian process [15] with the help of Busgang theorem. Hence, we use a generalized signal model [16], [17] to model the effect of these imperfections, which has been both theoretically and experimentally validated in [18]–[20]. Thus, the baseband equivalent received signal (1) can be expressed as

$$y = h_L h_P \mathbf{g}_1 \Phi \mathbf{g}_2 (x + n_S) + n_D + n, \quad (2)$$

where the parameters n_S and n_D are distortion noise from hardware impairments in both S and D [17], respectively, which can be defined as [17], [21]

$$n_S \sim \mathcal{CN}(0, \kappa_S^2 P), \quad (3)$$

$$n_D \sim \mathcal{CN}(0, \kappa_D^2 P |h_L h_P \mathbf{g}_1 \Phi \mathbf{g}_2|^2), \quad (4)$$

where κ_S and κ_D are non-negative parameters that characterize the level of hardware impairments [22] in S and D, respectively.

B. Small-Scale Measurement and Modeling of THz channel

The small-scale fading between BS and RIS is defined as

$$h_F \triangleq \mathbf{g}_1 \Phi \mathbf{g}_2, \quad (5)$$

where $\mathbf{g}_1 = [g_{1,1} e^{i\theta_{1,1}}, \dots, g_{L,1} e^{i\theta_{L,1}}]$ and $\mathbf{g}_2 = [g_{1,2} e^{i\theta_{1,2}}, \dots, g_{L,2} e^{i\theta_{L,2}}]^H$. Eq. (5) can be expressed as³

$$h_F = \sum_{\ell=1}^L e^{i(\varphi_\ell + \theta_{\ell,1} + \theta_{\ell,2})} g_{\ell,1} g_{\ell,2}. \quad (6)$$

Recently, the FTR fading channel [24] has received a great amount of research interest, because the FTR model yields a better fit than other conventional channel models with experimental data in high-frequency

³Typically, the electrical size of RIS elements is between $\lambda/8$ and $\lambda/4$, where λ is a wavelength of the signal [23]. This may cause channel correlation between the RIS-related channels. However, the exact correlation model at the RIS is still unknown through experiments or field trials. Thus, we assume that $g_{\ell,1}$ and $g_{\ell,2}$ are independent RVs.

communications. The FTR fading consists of two fluctuating specular components with random phases plus a diffuse component. The PDF of the squared FTR RV γ can be expressed as [25]

$$f_\gamma(\gamma) = \frac{m^m}{\Gamma(m)} \sum_{j=0}^{\infty} \frac{K^j d_j}{j!} f_G(\gamma; j+1, 2\sigma^2), \quad (7)$$

where

$$f_G(\gamma; j+1, 2\sigma^2) = \frac{\gamma^j}{\Gamma(j+1)(2\sigma^2)^{j+1}} \exp\left(-\frac{\gamma}{2\sigma^2}\right), \quad (8)$$

and

$$d_n \triangleq \sum_{k=0}^n \binom{n}{k} \left(\frac{\Delta}{2}\right)^k \sum_{l=0}^k \binom{k}{l} \Gamma(n+m+2l-k) e^{\frac{\pi(2l-k)j}{2}} \times ((m+K)^2 - (K\Delta)^2)^{\frac{-(n+m)}{2}} P_{n+m-1}^{k-2l} \left(\frac{m+K}{\sqrt{(m+K)^2 - (K\Delta)^2}} \right), \quad (9)$$

where $P(\cdot)$ denotes the Legendre function of the first kind [26, eq. (8.702)], $\gamma(\cdot, \cdot)$ is the incomplete gamma function [26, eq. (8.350.1)], m denotes the fading severity parameter, K is the average power ratio of the dominant wave to the scattering multipath, and Δ is a parameter varying from 0 to 1 representing the similarity of two dominant waves. Moreover, the received average SNR is given by $\nu = 2\sigma^2(1+K)$. Although the PDF and CDF expressions of the FTR RVs are infinite sums, we can use 40 terms to converge the series for all cases considered in this paper. Furthermore, note that the truncation error is less than 10^{-6} .

Very recently, a measurement campaign was conducted in a train test center with trains, tracks, and lampposts, which is highly similar to typical train-to-train scenarios. The authors use a novel, recently acquired M -sequence correlation-based ultrawideband channel sounder to measure the THz channel. In the measurement, the channel sounder was operated at 304.2 GHz with 8 GHz bandwidth. More details about the measurement campaign can be found in [11]. Based on the measurement data, the small scale fading was extracted for each channel impulse response (CIR).

We have fitted the measurement data to a Gaussian, Rician, Nakagami- m , and FTR distribution, respectively, which are also compared with the CDF of the measurement data. As shown in Fig. 2 and Fig. 3, we find that the FTR distribution performed a much better fit than other models. In the following, we use the FTR fading model to illustrate the small-scale amplitude fading of THz communications. Furthermore, a simple accurate single FTR approximation to the distribution of the sum of FTR RVs has

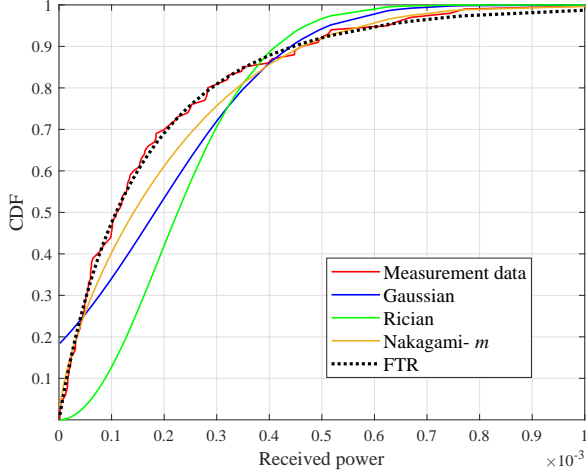


Fig. 2. CDF of the measurement data and fitted distributions.

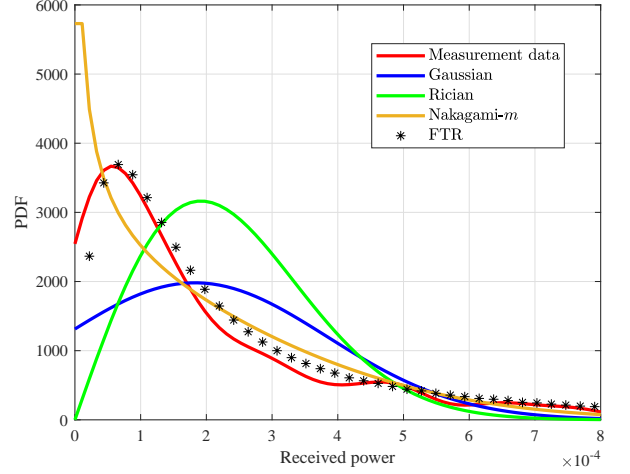


Fig. 3. PDF of the measurement data and fitted distributions.

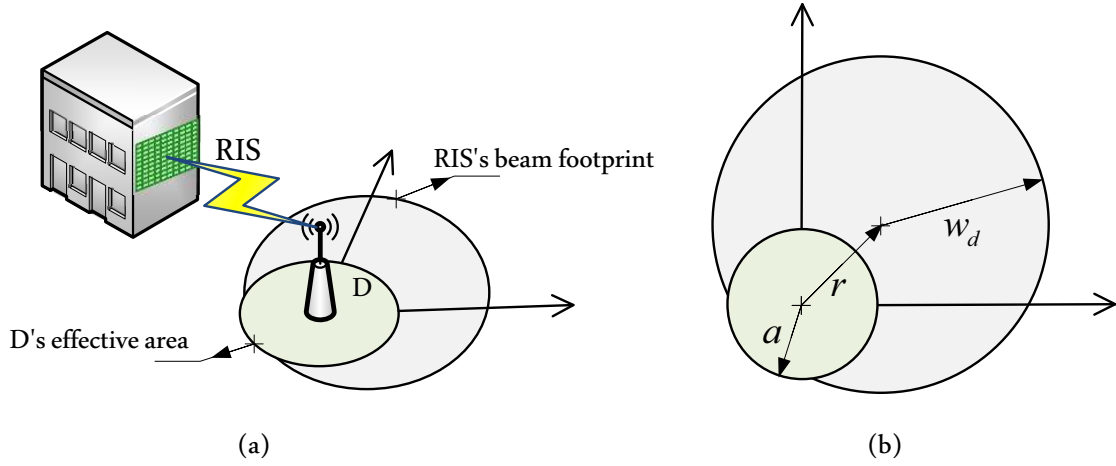


Fig. 4. D's effective area and RIS's beam footprint with misalignment.

been derived [13] with the help of the moment matching method and gradient descent algorithm. We can obtain the parameters of the single FTR distribution using [13, Algorithm 1]. Thus, our proposed analysis can be generalized to the case of multiple-antennas BS or user, because the FTR distribution we used in this paper can be regarded as the approximation to the distribution of the sum of FTR RVs.

C. Misalignment Fading Coefficient

In LoS communication links, pointing accuracy is an important issue in determining link performance and reliability. Prior works on RIS mostly consider the signal can be reflected towards D accurately. However, random building sways, which will be caused by wind loads and thermal expansions, will result in pointing errors and signal to fade at D.

As shown in Fig. 4, we consider that D has a circular detection beam that covers an area A , and the radius of the beam is α . Furthermore, the RIS has a circular beam of radius ρ , where $0 \leq \rho \leq \omega_d$, and ω_d denotes the maximum radius of the beam. Moreover, we assume that r is the pointing error expressed as the radial distance of the transmission and reception beams. Due to the symmetry of the beam shapes, the misalignment fading coefficient that represents the fraction of the power collected by D, h_P , depends only on the radial distance r . Thus, h_P can be approximated as [27, eq. (9)]

$$h_P(r; d) \approx A_o \exp\left(-\frac{2r^2}{w_{eq}^2}\right), \quad (10)$$

where w_{eq} is the equivalent beam-width and A_o is the fraction of the collected power at $r = 0$. Let $u \triangleq \sqrt{\pi}a/(\sqrt{2}w_d)$, where a is the radius of the D's effective area, and ω_d is the radius of the RIS's beam footprint at distance d_2 . Thus, w_{eq}^2 and A_o can be respectively calculated as

$$w_{eq}^2 = w_d^2 \frac{\sqrt{\pi} \operatorname{erf}(u)}{2u \exp(-u^2)}, \quad (11)$$

and

$$A_o = [\operatorname{erf}(u)]^2. \quad (12)$$

Considering independent identical Gaussian distributions for the elevation and horizontal displacement, the radial displacement at D can be modeled by a Rayleigh distribution as [27, eq. (10)]

$$f_r(r) = \frac{r}{\sigma_S^2} \exp\left(-\frac{r^2}{2\sigma_S^2}\right), \quad (13)$$

where σ_S^2 denotes the variance of the pointing error displacement at D. Combining (10) and (13), we can rewrite the PDF of h_P as

$$f_{h_P}(x) = \frac{\gamma^2}{A_o \gamma^2} x^{\gamma^2-1}, \quad 0 \leq x \leq A_o, \quad (14)$$

where $\gamma = \frac{w_{eq}}{2\sigma_s}$.

D. Path Gain Coefficient

The path gain coefficient can be evaluated as

$$h_L = h_{FL} h_{AL}, \quad (15)$$

where h_{FL} models the propagation gain, and h_{AL} denotes the molecular absorption gain. With the help of Friis equation, h_{FL} can be expressed as

$$h_{FL} = \frac{c\sqrt{G_t G_r}}{4\pi f (d_1 d_2)}, \quad (16)$$

where G_t and G_r represent the antenna orientation dependent transmission and reception gains, respectively. c is the speed of light, f stands for the operating frequency, d_1 is the distance between S and RIS, and d_2 is the distance between RIS and D. Furthermore, h_{AL} can be evaluated as [7]

$$h_{AL} = \exp\left(-\frac{1}{2}\kappa_\alpha(f)(d_1 + d_2)\right), \quad (17)$$

where $\kappa_\alpha(f)$ denotes the absorption coefficient. Many methods has been used to evaluate the molecular absorption coefficient [7], [28]. In [7], authors proposed a molecular absorption model that is valid at 275-400 GHz frequency band. This molecular absorption model is also equally accurate from 200 to 400 GHz. Thus, it is suitable to model the band that THz fiber extenders are expected to operate in. With the help of this absorption model, $\kappa_\alpha(f)$ can be expressed as

$$\kappa_\alpha(f) = y_1(f, v) + y_2(f, v) + g(f), \quad (18)$$

where the parameters $y_1(f, v)$, $y_2(f, v)$ and $g(f)$ are given as [7]

$$y_1(f, v) = \frac{A(v)}{B(v) + \left(\frac{f}{100c} - c_1\right)^2}, \quad (19)$$

$$y_2(f, v) = \frac{C(v)}{D(v) + \left(\frac{f}{100c} - c_2\right)^2}, \quad (20)$$

and

$$g(f) = p_1 f^3 + p_2 f^2 + p_3 f + p_4, \quad (21)$$

where c denotes the speed of light, $c_1 = 10.835 \text{ cm}^{-1}$, $c_2 = 12.664 \text{ cm}^{-1}$, $p_1 = 5.54 \times 10^{-37} \text{ Hz}^{-3}$, $p_2 = -3.94 \times 10^{-25} \text{ Hz}^{-2}$, $p_3 = 9.06 \times 10^{-14} \text{ Hz}^{-1}$, $p_4 = -6.36 \times 10^{-3}$, $A(v) = 0.2205v(0.1303v + 0.0294)$, $B(v) = (0.4093v + 0.0925)^2$, $C(v) = 2.014v(0.1702v + 0.0303)$, and $D(v) = (0.537v + 0.0956)^2$.

Moreover, v can be evaluated as

$$v = \frac{\phi}{100} \frac{p_w(T, p)}{p}, \quad (22)$$

where T is the temperature, ϕ and p denote the relative humidity and the atmospheric pressure, respectively. $p_w(T, p)$ stands for the saturated water vapor partial pressure. With the help of Buck's equation, $p_w(T, p)$ can be calculated as

$$p_w(T, p) = 6.1121 (1.0007 + 3.46 \times 10^{-6} p) \exp\left(\frac{17.502T}{240.97 + T}\right). \quad (23)$$

Using (15)-(23), we finally obtain the path gain coefficient of the considered RIS-aided THz communication system.

III. PHASE SHIFT DESIGN UNDER DISCRETE PHASE SHIFT CONSTRAINTS

A. Optimal Phase Shift Design of RIS's Reflector Elements

Maximizing the SNR is equivalent to maximizing $|h_F|$. With the help of (6), we can express $|h_F|$ as

$$|h_F| = \left| \sum_{\ell=1}^L e^{i(\varphi_\ell + \theta_{\ell,1} + \theta_{\ell,2})} g_{\ell,1} g_{\ell,2} \right| \leq \left| \sum_{\ell=1}^L g_{\ell,1} g_{\ell,2} \right|, \quad (24)$$

where φ_ℓ is the adjustable phase induced by the i_{th} reflecting element of the RIS. The optimal choice of φ_ℓ can maximize the instantaneous SNR by letting $\theta_{\ell,1} + \theta_{\ell,2} + \varphi_\ell = \phi$ for all i [4, eq. (12)], where ϕ is a constant phase.

However, eliminating the channel phases is difficult because the RIS is assumed to be passive. Recently, a novel and simple algorithm based on the binary search tree was proposed to obtain Φ_{opt} without the channel phases information [29]. By maximizing the expectation of the amplitude of the received signal, the optimal choice of φ_ℓ can be obtained. However, the algorithm proposed in [29] is based on assuming the phase-shifts is continuous at each reflecting element, which is practically difficult to realize due to the hardware limitation of the RIS. Obviously, the design of RIS hardware and control module can be simplified by using discrete phase shifters. Thus, in contrast to the continuous phase-shifts, we consider the practical case where the RIS only has a finite number of discrete phase-shifts that are equally spaced in $[0, 2\pi)$. The set of phase-shifts at each element is given by

$$\mathcal{O} = \{0, \Delta\theta, \dots, \Delta\theta(K-1)\}, \quad (25)$$

where $\Delta\theta = 2\pi/K$ and $K = \lceil \frac{2\pi}{\Delta\theta} \rceil$. If we use b bits to represent each of the levels, we can also express K as $K = 2^b$. Note that the maximum achievable expectation of the amplitude of the received signal can

be written as

$$\mathbb{E} [|h_L| |h_P| |h_F|] = |h_L| \mathbb{E} [|h_P|] \mathbb{E} \left[\left| \sum_{\ell=1}^L e^{i(\varphi_\ell + \theta_{\ell,1} + \theta_{\ell,2})} g_{\ell,1} g_{\ell,2} \right| \right] \leq |h_L| \mathbb{E} [|h_P|] \mathbb{E} \left[\left| \sum_{\ell=1}^L g_{\ell,1} g_{\ell,2} \right| \right], \quad (26)$$

where $\mathbb{E}[\cdot]$ denotes the mathematical expectation.

Let $E_{\text{re}} = \mathbb{E} [|h_L| |h_P| |h_F|]$ and $E_{\text{opt}} = |h_L| \mathbb{E} [|h_P|] \mathbb{E} \left[\left| \sum_{\ell=1}^L g_{\ell,1} g_{\ell,2} \right| \right]$, where E_{re} can be easily measured in the time domain and E_{opt} can be obtained as

$$E_{\text{opt}} = \frac{|h_L| \gamma^2 A_o}{\gamma^2 + 1} \sum_{\ell=1}^L \prod_{\ell=1}^2 \frac{m_\ell^{m_\ell}}{\Gamma(m_\ell)} \sum_{j_\ell=0}^{\infty} \frac{K_\ell^{j_\ell} d_{\ell,j_\ell}}{j_\ell!} \frac{(2\sigma_\ell^2)^{\frac{1}{2}}}{\Gamma(j_\ell + 1)} \Gamma\left(\frac{3}{2} + j_\ell\right). \quad (27)$$

Proof: With the help of [29, eq. (6)], $\mathbb{E} \left[\left| \sum_{\ell=1}^L g_{\ell,1} g_{\ell,2} \right| \right]$ can be expressed as

$$\mathbb{E} \left[\left| \sum_{\ell=1}^L g_{\ell,1} g_{\ell,2} \right| \right] = \sum_{\ell=1}^L \prod_{\ell=1}^2 \frac{m_\ell^{m_\ell}}{\Gamma(m_\ell)} \sum_{j_\ell=0}^{\infty} \frac{K_\ell^{j_\ell} d_{\ell,j_\ell}}{j_\ell!} \frac{(2\sigma_\ell^2)^{\frac{1}{2}}}{\Gamma(j_\ell + 1)} \Gamma\left(\frac{3}{2} + j_\ell\right). \quad (28)$$

The s_{th} moment of $|h_P|$ is defined as

$$E [|h_P|^s] = \int_0^{A_o} x^s f_{h_p}(x) dx. \quad (29)$$

Substituting (14) into (29), we obtain

$$E [|h_P|^s] = \frac{\gamma^2}{A_o^{\gamma^2}} \int_0^{A_o} x^{\gamma^2+s-1} dx = \frac{\gamma^2}{\gamma^2 + s} A_o^s. \quad (30)$$

By substituting $s = 1$ into (30), $E [|h_P|]$ is derived. Thus, we obtain (27) which completes the proof. ■

Combining the above discussion, we present Algorithm 1 to find Φ_{opt} for the RIS with finite-level phase-shifters. Note that $\text{Mod}[a, b]$ denotes the remainder on division of a by b . In a real RIS-aided THz communication system, Φ_{opt} can be obtained by adjusting φ_ℓ and measuring the expectation of the amplitude of the received signal, E_{re} . E_{opt} is only used to test the effectiveness of our algorithm in simulation experiments. The convergence and effectiveness of the algorithm, even when the size of the RIS is large, has been verified in [29] with the continuous phase-shifts ($\Delta\theta \rightarrow 0$). Furthermore, Algorithm 1 can be regarded as iterations of binary search tree algorithms. Therefore, for each iteration, the complexity is shown as $\mathcal{O}(\log_2(K))$.

Algorithm 1 The binary search tree algorithm to find Φ_{opt} for the RIS with finite-level phase-shifters.

Input: Input the number of elements on RIS: L , the minimum value of phase-shifts: $\Delta\theta$, the maximum achievable expectation: E_{opt} and E_ℓ ($\ell = 1, \dots, L$), iteration numbers: M_1 and M_2

Output: The phase-shift variable ϕ_ℓ ($\ell = 1, \dots, L$) for each RIS element should be set.

- 1: Initialize $\phi_{\text{LB}} = 0$, $\phi_{\text{UB}} = \pi$ and $\ell_{\text{th}} = 1$. Set iteration index $\text{LP}_1 = \text{LP}_2 = t = 0$.
 - 2: **while** $\text{LP}_2 < M_2$ **do**
 - 3: **while** $\ell_{\text{th}} \leq L$ **do**
 - 4: **while** $\text{LP}_1 < M_1$ **do**
 - 5: When the phase-shift variable of the ℓ_{th} elements is set as ϕ_{LB} and ϕ_{UB} , we use E_{m_1} and E_{m_2} to denote the expectation of the amplitude of the received signal measured at the user, respectively.
 - 6: $t \leftarrow t + 1$
 - 7: **if** $E_{m_1} > E_{m_2}$ **then**
 - 8: $\phi_{\text{LB}} \leftarrow \text{Mod} \left[\phi_{\text{LB}} + \frac{\pi}{2^{t+1}} + 1, 2\pi \right]$ and $\phi_{\text{LB}} \leftarrow [\phi_{\text{LB}}/\Delta\theta] \times \Delta\theta$,
 - 9: $\phi_{\text{UB}} \leftarrow \text{Mod} \left[\phi_{\text{UB}} - \frac{\pi}{2^t}, 2\pi \right]$ and $\phi_{\text{UB}} \leftarrow [\phi_{\text{UB}}/\Delta\theta] \times \Delta\theta$.
 - 10: **else**
 - 11: $\phi_{\text{UB}} \leftarrow \text{Mod} \left[\phi_{\text{UB}} + \frac{\pi}{2^{t+1}}, 2\pi \right]$ and $\phi_{\text{UB}} \leftarrow [\phi_{\text{UB}}/\Delta\theta] \times \Delta\theta$,
 - 12: $\phi_{\text{LB}} \leftarrow \text{Mod} \left[\phi_{\text{LB}} - \frac{\pi}{2^t}, 2\pi \right]$ and $\phi_{\text{LB}} \leftarrow [\phi_{\text{LB}}/\Delta\theta] \times \Delta\theta$.
 - 13: $\text{LP}_1 \leftarrow \text{LP}_1 + 1$
 - 14: $\ell_{\text{th}} \leftarrow \ell_{\text{th}} + 1$, $t \leftarrow 0$ and $\text{LP}_1 \leftarrow 0$.
 - 15: $\text{LP}_2 \leftarrow \text{LP}_2 + 1$, $\phi_\ell \leftarrow \text{Mod} [\phi_\ell + \phi_{\text{LB}}]$, $\phi_{\text{LB}} \leftarrow 0$ and $\phi_{\text{UB}} \leftarrow 0$
 - 16: **return** ϕ_ℓ ($\ell = 1, \dots, L$)
-

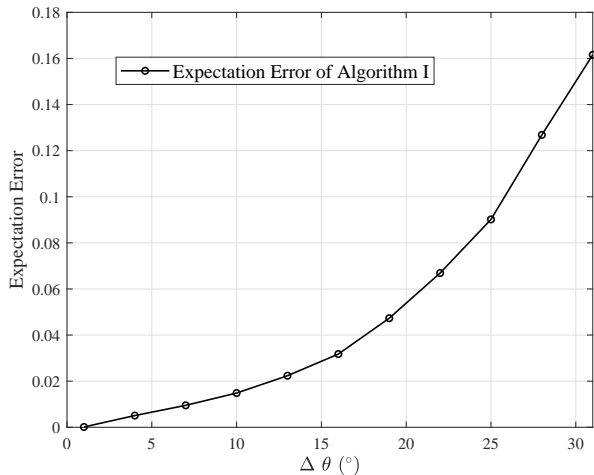


Fig. 5. The expectation error of the proposed phase optimization method.

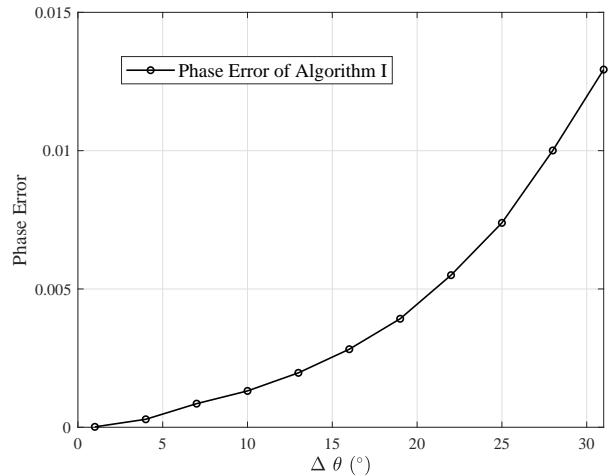


Fig. 6. The phase error of the proposed phase optimization method.

B. Impact of Different Number of Discrete Phase Shift Levels

We focus on investigating the impact of different number of discrete phase-shifts levels. We define $\zeta \triangleq E_{\text{opt}} - E_{\text{re}}$ to characterize the error of expectation, and we use the variance of $\theta_{\ell,1} + \theta_{\ell,2} + \phi_\ell$ ($\ell = 1, \dots, L$) to show the phase error.

In Figs. 5 and 6, we verify the effectiveness of the proposed algorithm with 100 simulation experiments with $M_1 = 11$, $M_2 = 5$ and random initial phase, $\theta_{1,1}$, $\theta_{1,2}$, $\theta_{2,1}$, $\theta_{2,2}$, $\theta_{3,1}$, and $\theta_{3,2}$, for every choice of $\Delta\theta$. Figures 5 and 6, respectively, plot an example of the expectation and phase error, assuming $L = 3$, $m_{1,1} = m_{1,2} = 10$, $K_{1,1} = K_{1,2} = 3$, $v_{1,1} = v_{1,2} = 10$, $\Delta_{1,1} = \Delta_{1,2} = 0.5$, $m_{2,1} = m_{2,2} = 5$, $K_{2,1} = K_{2,2} = 5$, $v_{2,1} = v_{2,2} = 20$, $\Delta_{2,1} = \Delta_{2,2} = 0.5$, $m_{3,1} = m_{3,2} = 15$, $K_{3,1} = K_{3,2} = 1$, $v_{3,1} = v_{3,2} = 10$ and $\Delta_{3,1} = \Delta_{3,2} = 0.3$. We calculate the average expectation and phase error of 100 random initial phases to obtain Figs. 5 and 6, and we can observe that the error of expectation and the phase error increase as $\Delta\theta$ is increased. In addition, we observe that even using the RIS with large $\Delta\theta$ is able to achieve close power gain to when using RIS with continuous phase-shifts (e.g., the expectation error is less than 0.17 and the phase error is less than 0.015). Furthermore, for once specific simulation experiment, an interesting insight is that we may obtain smaller expectation and phase error when $\Delta\theta$ is larger, which is because the possible values of phase-shifts under a large $\Delta\theta$ may contain the optimal choice. As shown in Fig. 7, $\Delta\theta = \pi/2$ is better than $\Delta\theta = \pi/3$.

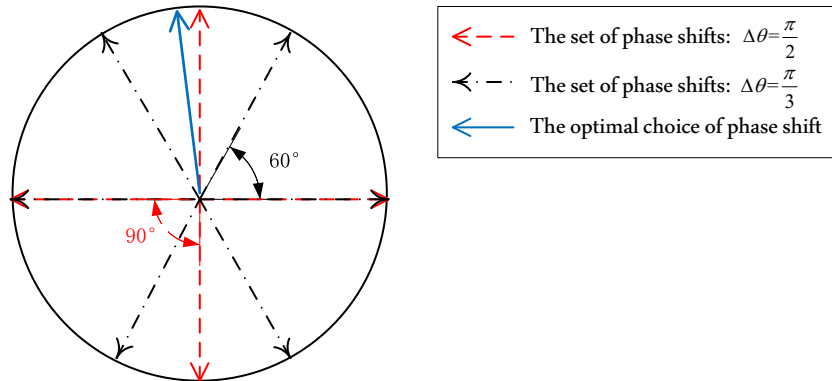


Fig. 7. The reason why a RIS with a larger $\Delta\theta$ can obtain larger SNR.

IV. EXACT STATISTICS OF THE END-TO-END SNR AND SNDR

Substituting $R = \sqrt{\gamma}$ into (7), we can easily obtain the PDF expression of FTR RVs. Let $Y = \sum_{\iota=1}^L \prod_{\ell=1}^N R_{\iota,\ell}$ as the sum of product of N FTR RVs, where $R_{\iota,\ell} \sim \mathcal{FTR}(K_{\iota,\ell}, m_{\iota,\ell}, \Delta_{\iota,\ell}, \sigma_{\iota,\ell}^2)$ ($\iota = 1, \dots, L$ and $\ell = 1, \dots, N$), the exact PDF and CDF of Y have been respectively derived as [29, eq. 11] and [29, eq.

12]

$$f_Y(y) = \sum_{j_{1,1}, \dots, j_{L,1}=0}^{\infty} \dots \sum_{j_{1,N}, \dots, j_{L,N}=0}^{\infty} \prod_{\ell=1}^L \prod_{\ell=1}^N \frac{K_{\ell, \ell}^{j_{\ell, \ell}} d_{\ell, \ell}^{j_{\ell, \ell}} m_{\ell, \ell}^{m_{\ell, \ell}}}{j_{\ell, \ell}!} \frac{1}{\Gamma(m_{\ell, \ell})} \frac{1}{\Gamma(j_{\ell, \ell} + 1)} \frac{1}{y}$$

$$\times H_{1,0:N,1;\dots;N,1}^{0,0:1,N;\dots;1,N} \left(\begin{array}{c} y^{-1} \prod_{\ell=1}^N (\sqrt{2}\sigma_{1,\ell}) \\ \vdots \\ y^{-1} \prod_{\ell=1}^N (\sqrt{2}\sigma_{L,\ell}) \end{array} \middle| \begin{array}{c} (0; 1, \dots, 1) : \{(-j_{1,n}, 0.5)\}_1^N; \dots; \{(-j_{L,n}, 0.5)\}_1^N \\ - : (0, 1); \dots; (0, 1) \end{array} \right), \quad (31)$$

$$F_Y(y) = \sum_{j_{1,1}, \dots, j_{L,1}=0}^{\infty} \dots \sum_{j_{1,N}, \dots, j_{L,N}=0}^{\infty} \prod_{\ell=1}^L \prod_{\ell=1}^N \frac{K_{\ell, \ell}^{j_{\ell, \ell}} d_{\ell, \ell}^{j_{\ell, \ell}} m_{\ell, \ell}^{m_{\ell, \ell}}}{j_{\ell, \ell}!} \frac{1}{\Gamma(m_{\ell, \ell})} \frac{1}{\Gamma(j_{\ell, \ell} + 1)}$$

$$\times H_{1,0:N,1;\dots;N,1}^{0,0:1,N;\dots;1,N} \left(\begin{array}{c} y^{-1} \prod_{\ell=1}^N (\sqrt{2}\sigma_{1,\ell}) \\ \vdots \\ y^{-1} \prod_{\ell=1}^N (\sqrt{2}\sigma_{L,\ell}) \end{array} \middle| \begin{array}{c} (1; 1, \dots, 1) : \{(-j_{1,n}, 0.5)\}_1^N; \dots; \{(-j_{L,n}, 0.5)\}_1^N \\ - : (0, 1); \dots; (0, 1) \end{array} \right), \quad (32)$$

where $\{(a_n)\}_1^N = (a_1), \dots, (a_N)$.

Note that the multivariable Fox's H function is defined in terms of multiple Mellin-Barnes type contour integral as [30, eq. (A.1)]

$$H[z_1, \dots, z_r] = H_{p,q;p_1,q_1;\dots;p_r,q_r}^{0,n:m_1,n_1;\dots;m_r,n_r} \left[\begin{array}{c} z_1 \\ \vdots \\ z_r \end{array} \middle| \begin{array}{c} (a_j; \alpha_j^{(1)}, \dots, \alpha_j^{(r)})_{1,p} : (c_j^{(1)}, \gamma_j^{(1)})_{1,p_1}; \dots; (c_j^{(r)}, \gamma_j^{(r)})_{1,p_r} \\ (b_j; \beta_j^{(1)}, \dots, \beta_j^{(r)})_{1,q} : (d_j^{(1)}, \delta_j^{(1)})_{1,q_1}; \dots; (d_j^{(r)}, \delta_j^{(r)})_{1,q_r} \end{array} \right]$$

$$= \frac{1}{(2\pi w)^r} \int_{L_1} \dots \int_{L_r} \Psi(\zeta_1, \dots, \zeta_r) \left\{ \prod_{i=1}^r \phi_i(\zeta_i) z_i^{\zeta_i} \right\} d\zeta_1 \dots d\zeta_r, \quad (33)$$

where

$$\Psi(\zeta_1, \dots, \zeta_r) = \frac{\prod_{j=1}^n \Gamma\left(1 - a_j + \sum_{i=1}^r \alpha_j^{(i)} \zeta_i\right)}{\prod_{j=n+1}^p \Gamma\left(a_j - \sum_{i=1}^r \alpha_j^{(i)} \zeta_i\right) \prod_{j=1}^q \Gamma\left(1 - b_j + \sum_{i=1}^r \beta_j^{(i)} \zeta_i\right) B}, \quad (34)$$

$$\phi_i(\zeta_i) = \frac{\prod_{\lambda=1}^{m_i} \Gamma\left(d_\lambda^{(i)} - \delta_\lambda^{(i)} \zeta_i\right) \prod_{j=1}^{n_i} \Gamma\left(1 - c_j^{(i)} + \gamma_j^{(i)} \zeta_i\right)}{\prod_{j=n_i+1}^{p_i} \Gamma\left(c_j^{(i)} - \gamma_j^{(i)} \zeta_i\right) \prod_{\lambda=m_i+1}^{q_i} \Gamma\left(1 - d_\lambda^{(i)} + \delta_\lambda^{(i)} \zeta_i\right)}. \quad (35)$$

We have verified that Algorithm 1 can be used to obtain the phase-shifts of RIS's elements which enable

the received power tightly close to the optimal received power. Then, we present the instantaneous optimal SNR and SNDR for the case of ideal and non-ideal RF chains, respectively.

A. Non-Ideal RF Chains

The instantaneous SNDR can be expressed as

$$\gamma_N = \frac{|h_{FP}|^2 |h_L|^2 P}{\kappa^2 |h_{FP}|^2 |h_L|^2 P + N_o}, \quad (36)$$

where $\kappa^2 \triangleq \kappa_S^2 + \kappa_D^2$. To derive a generic analytical expression for the CDF of the instantaneous SNDR of non-ideal RF chains, we first present the following useful Lemma.

Lemma 1. *Considering hardware impairments, we derive an integral representation for the PDF and CDF of γ_N in (36) assuming arbitrarily distributed $|h_F|$ and $|h_P|$ as*

$$f_{\gamma_N}(x) = \frac{1}{2\sqrt{x(1-x\kappa^2)}^3 \frac{|h_L|^2 P}{N_o}} \int_0^{A_o} \frac{1}{y} f_{|h_F|} \left(\frac{1}{y} \sqrt{\frac{xN_o}{|h_L|^2 P (1-x\kappa^2)}} \right) f_{|h_P|}(y) dy, \quad (37)$$

$$F_{\gamma_N}(x) = \int_0^{A_o} F_{|h_F|} \left(\frac{1}{y} \sqrt{\frac{xN_o}{|h_L|^2 P (1-x\kappa^2)}} \right) f_{|h_P|}(y) dy. \quad (38)$$

Proof: Please refer to Appendix A. ■

With the help of Lemma 1, for special distributed $|h_F|$ and $|h_P|$ in this paper, we first derive the PDF and CDF of $|h_{FP}|$ as

Theorem 1. *The PDF and CDF of $|h_{FP}| \triangleq |h_F| \times |h_P|$ can be expressed as*

$$f_{|h_{FP}|}(x) = \sum_{j_{1,1}, \dots, j_{L,1}=0}^{\infty} \sum_{j_{1,2}, \dots, j_{L,2}=0}^{\infty} \prod_{\iota=1}^L \prod_{\ell=1}^2 \frac{K_{\iota,\ell}^{j_{\iota,\ell}} d_{\iota,\ell}^{j_{\iota,\ell}} m_{\iota,\ell}^{m_{\iota,\ell}}}{j_{\iota,\ell}!} \frac{1}{\Gamma(m_{\iota,\ell}) \Gamma(j_{\iota,\ell} + 1)} \frac{\gamma^2}{x} \\ \times H_{1,0:3,2; \dots; 3,2}^{0,0:1,3; \dots; 1,3} \left(\begin{array}{c} \frac{A_0}{x} \prod_{\ell=1}^2 (\sqrt{2}\sigma_{1,\ell}) \\ \vdots \\ \frac{A_0}{x} \prod_{\ell=1}^2 (\sqrt{2}\sigma_{L,\ell}) \end{array} \middle| \begin{array}{c} (0; 1, \dots, 1) : \nu_{h_{FP},1}; \dots; \nu_{h_{FP},L} \\ - : (0, 1), (-\gamma^2, 1); \dots; (0, 1), (-\gamma^2, 1) \end{array} \right), \quad (39)$$

$$\begin{aligned}
F_{|h_{FP}|}(x) = & \sum_{j_{1,1}, \dots, j_{L,1}=0}^{\infty} \sum_{j_{1,2}, \dots, j_{L,2}=0}^{\infty} \prod_{\iota=1}^L \prod_{\ell=1}^2 \frac{K_{\iota,\ell}^{j_{\iota,\ell}} d_{\iota,\ell}^{j_{\iota,\ell}} m_{\iota,\ell}^{m_{\iota,\ell}}}{j_{\iota,\ell}!} \frac{1}{\Gamma(m_{\iota,\ell}) \Gamma(j_{\iota,\ell} + 1)} \gamma^2 \\
& \times H_{1,0:3,2; \dots; 3,2}^{0,0:1,3; \dots; 1,3} \left(\begin{array}{c} \frac{A_0}{x} \prod_{\ell=1}^2 (\sqrt{2}\sigma_{1,\ell}) \\ \vdots \\ \frac{A_0}{x} \prod_{\ell=1}^2 (\sqrt{2}\sigma_{L,\ell}) \end{array} \middle| \begin{array}{l} (1; 1, \dots, 1) : \nu_{h_{FP},1}; \dots; \nu_{h_{FP},L} \\ - : (0, 1), (-\gamma^2, 1); \dots; (0, 1), (-\gamma^2, 1) \end{array} \right), \quad (40)
\end{aligned}$$

where $\nu_{h_{FP},\ell} = \{(-j_{\ell,n}, 0.5)\}_1^2, (1 - \gamma^2, 1)$ ($\ell = 1, \dots, L$).

Proof: Please refer to Appendix B. ■

Therefore, the statistics of instantaneous SNDR can be obtained as the following Theorem

Theorem 2. *The PDF and CDF of γ_N can be derived as*

$$\begin{aligned}
f_{\gamma_N}(x) = & \sum_{j_{1,1}, \dots, j_{L,1}=0}^{\infty} \sum_{j_{1,2}, \dots, j_{L,2}=0}^{\infty} \prod_{\iota=1}^L \prod_{\ell=1}^2 \frac{K_{\iota,\ell}^{j_{\iota,\ell}} d_{\iota,\ell}^{j_{\iota,\ell}} m_{\iota,\ell}^{m_{\iota,\ell}}}{j_{\iota,\ell}!} \frac{\gamma^2}{\Gamma(m_{\iota,\ell}) \Gamma(j_{\iota,\ell} + 1)} \frac{1}{2x(1 - x\kappa^2)} \\
& \times H_{1,0:3,2; \dots; 3,2}^{0,0:1,3; \dots; 1,3} \left(\begin{array}{c} A_0 \sqrt{\frac{|h_L|^2 P(1-x\kappa^2)}{xN_o}} \prod_{\ell=1}^2 (\sqrt{2}\sigma_{1,\ell}) \\ \vdots \\ A_0 \sqrt{\frac{|h_L|^2 P(1-x\kappa^2)}{xN_o}} \prod_{\ell=1}^2 (\sqrt{2}\sigma_{L,\ell}) \end{array} \middle| \begin{array}{l} (0; 1, \dots, 1) : \nu_{h_{FP},1}; \dots; \nu_{h_{FP},L} \\ - : (0, 1), (-\gamma^2, 1); \dots; (0, 1), (-\gamma^2, 1) \end{array} \right), \quad (41)
\end{aligned}$$

$$\begin{aligned}
F_{\gamma_N}(x) = & \sum_{j_{1,1}, \dots, j_{L,1}=0}^{\infty} \sum_{j_{1,2}, \dots, j_{L,2}=0}^{\infty} \prod_{\iota=1}^L \prod_{\ell=1}^2 \frac{K_{\iota,\ell}^{j_{\iota,\ell}} d_{\iota,\ell}^{j_{\iota,\ell}} m_{\iota,\ell}^{m_{\iota,\ell}}}{j_{\iota,\ell}!} \frac{1}{\Gamma(m_{\iota,\ell}) \Gamma(j_{\iota,\ell} + 1)} \gamma^2 \\
& \times H_{1,0:3,2; \dots; 3,2}^{0,0:1,3; \dots; 1,3} \left(\begin{array}{c} A_0 \sqrt{\frac{|h_L|^2 P(1-x\kappa^2)}{xN_o}} \prod_{\ell=1}^2 (\sqrt{2}\sigma_{1,\ell}) \\ \vdots \\ A_0 \sqrt{\frac{|h_L|^2 P(1-x\kappa^2)}{xN_o}} \prod_{\ell=1}^2 (\sqrt{2}\sigma_{L,\ell}) \end{array} \middle| \begin{array}{l} (1; 1, \dots, 1) : \nu_{h_{FP},1}; \dots; \nu_{h_{FP},L} \\ - : (0, 1), (-\gamma^2, 1); \dots; (0, 1), (-\gamma^2, 1) \end{array} \right). \quad (42)
\end{aligned}$$

Proof: With the help of (37), (38), (39), and (40), the PDF and CDF of γ_N can be easily obtained after performing some mathematical manipulations, which completes the proof. ■

Remark 1. *The multivariable Fox's H function can not be evaluated directly by popular mathematical packages in MATLAB or Mathematica. However, many implementations have been proposed [31]–[34]. In the following, we use an efficient and accurate Python implementation [33] that can provide numerical results of multivariable Fox's H function in a few seconds. Moreover, the CDF expression of $|h_{FP}|$ has the similar formula as that of the sum of product of FTR RVs, and the truncation error of Y has been*

presented to show the effect of infinite series on the performance of the CDF expression. With a satisfactory accuracy (e.g., smaller than 10^{-5}), only a few terms (e.g., less than 30) are needed for all considered cases.

B. Ideal RF Chains

Let us consider the case of ideal RF chains. With the help of (1), we can express the instantaneous SNR of the received signal as

$$\gamma_I = \frac{|h_{FP}|^2 |h_L|^2 P}{N_o}. \quad (43)$$

Theorem 3. *The PDF and CDF of γ_I can be derived as*

$$f_{\gamma_I}(x) = \sum_{j_{1,1}, \dots, j_{L,1}=0}^{\infty} \sum_{j_{1,2}, \dots, j_{L,2}=0}^{\infty} \prod_{\ell=1}^L \prod_{\ell=1}^2 \frac{K_{\ell, \ell}^{j_{\ell, \ell}} d_{\ell, \ell}^{j_{\ell, \ell}} m_{\ell, \ell}^{m_{\ell, \ell}}}{j_{\ell, \ell}!} \frac{\gamma^2}{\Gamma(m_{\ell, \ell}) \Gamma(j_{\ell, \ell} + 1)} \frac{1}{2x} \\ \times H_{1,0:3,2; \dots; 3,2}^{0,0:1,3; \dots; 1,3} \left(\begin{array}{c} A_0 \sqrt{\frac{|h_L|^2 P}{x N_o}} \prod_{\ell=1}^2 (\sqrt{2} \sigma_{1, \ell}) \\ \vdots \\ A_0 \sqrt{\frac{|h_L|^2 P}{x N_o}} \prod_{\ell=1}^2 (\sqrt{2} \sigma_{L, \ell}) \end{array} \middle| \begin{array}{l} (0; 1, \dots, 1) : v_{h_{FP,1}}; \dots; v_{h_{FP,L}} \\ - : (0, 1), (-\gamma^2, 1); \dots; (0, 1), (-\gamma^2, 1) \end{array} \right), \quad (44)$$

$$F_{\gamma_I}(x) = \sum_{j_{1,1}, \dots, j_{L,1}=0}^{\infty} \sum_{j_{1,2}, \dots, j_{L,2}=0}^{\infty} \prod_{\ell=1}^L \prod_{\ell=1}^2 \frac{K_{\ell, \ell}^{j_{\ell, \ell}} d_{\ell, \ell}^{j_{\ell, \ell}} m_{\ell, \ell}^{m_{\ell, \ell}}}{j_{\ell, \ell}!} \frac{1}{\Gamma(m_{\ell, \ell}) \Gamma(j_{\ell, \ell} + 1)} \gamma^2 \\ \times H_{1,0:3,2; \dots; 3,2}^{0,0:1,3; \dots; 1,3} \left(\begin{array}{c} A_0 \sqrt{\frac{|h_L|^2 P}{x N_o}} \prod_{\ell=1}^2 (\sqrt{2} \sigma_{1, \ell}) \\ \vdots \\ A_0 \sqrt{\frac{|h_L|^2 P}{x N_o}} \prod_{\ell=1}^2 (\sqrt{2} \sigma_{L, \ell}) \end{array} \middle| \begin{array}{l} (1; 1, \dots, 1) : v_{h_{FP,1}}; \dots; v_{h_{FP,L}} \\ - : (0, 1), (-\gamma^2, 1); \dots; (0, 1), (-\gamma^2, 1) \end{array} \right). \quad (45)$$

Proof: Substituting $\kappa^2 = 0$ into (39) and (40), we obtain the PDF and CDF of γ_N after performing some mathematical manipulations, which completes the proof. ■

The statistics of γ_I and γ_N we derived in Theorem 2 and Theorem 3 can be used to obtain exact closed-form expressions for key performance metrics.

V. PERFORMANCE ANALYSIS

A. Outage Probability

The outage probability P can be defined as the probability that the received SNR per signal falls below a given threshold γ_{th} . Thus, the OP of considered THz communications can be obtained as

$$P_{out} = P(\gamma_\ell < \gamma_{th}) = F_{\gamma_\ell}(\gamma_{th}), \quad (46)$$

where $\ell \in N, I$. for the case of non-ideal RF chains, the OP of the RIS-aided system can be directly obtained by using (42). Furthermore, we can obtain the OP for the case of ideal RF chains with the help of (45). Thus, we can observe that a RIS equipped with more reflecting elements will also make the OP lower.

B. Ergodic Capacity

Channel capacity is an important performance metric in wireless communication systems. Furthermore, ergodic capacity is the most widely used capacity measure. The ergodic capacity under optimal rate adaptation with constant transmit power is given by [35, eq. (29)]

$$C = \mathbb{E}[\log_2(1 + \gamma_\ell)], \quad (47)$$

where $\ell \in N, I$.

1) *Non-Ideal RF Chains*: for the case of non-ideal RF chains, the exact expression of the ergodic capacity is hard to be derived due to the complexity of (41). However, the following theorem returns a closed-form upper bound of the ergodic capacity, which can lead to more generic, and practically more useful and reliable results.

Proposition 1. *The effective capacity of the RIS-aid THz communications for the case of non-ideal RF chains is bounded by*

$$C_N \leq \log_2 \left(1 + \frac{P|h_L|^2 \mathbb{E}[|h_{FP}|^2]}{P\kappa^2|h_L|^2 \mathbb{E}[|h_{FP}|^2] + N_o} \right), \quad (48)$$

where

$$\mathbb{E} [|h_{FP}|^2] = \sum_{j_{1,1}, \dots, j_{L,1}=0}^{\infty} \sum_{j_{1,2}, \dots, j_{L,2}=0}^{\infty} \prod_{\iota=1}^L \prod_{\ell=1}^2 \frac{K_{\iota,\ell}^{j_{\iota,\ell}} d_{\iota,\ell}^{j_{\iota,\ell}} m_{\iota,\ell}^{m_{\iota,\ell}}}{j_{\iota,\ell}! \Gamma(m_{\iota,\ell})} \frac{\gamma^2}{e^2 \Gamma(j_{\iota,\ell} + 1)}$$

$$\times H_{2,0:3,2; \dots; 3,2}^{0,1:1,3; \dots; 1,3} \left(\begin{array}{c} eA_0 \prod_{\ell=1}^2 (\sqrt{2}\sigma_{1,\ell}) \\ \vdots \\ eA_0 \prod_{\ell=1}^2 (\sqrt{2}\sigma_{L,\ell}) \end{array} \middle| \begin{array}{l} (-1; -1, \dots, -1), (0; -1, \dots, -1) : v_{FP,1}; \dots; v_{FP,L} \\ - : (0, 1), (-\gamma^2, 1); \dots; (0, 1), (-\gamma^2, 1) \end{array} \right). \quad (49)$$

Proof: Please refer to Appendix C. ■

2) *Ideal RF Chains:* For the case of ideal RF chains, we can derive the exact expression of the ergodic capacity using (47).

Proposition 2. *The effective capacity of the RIS-aid system for the case of ideal RF chains can be derived as*

$$C = \sum_{j_{1,1}, \dots, j_{L,1}=0}^{\infty} \sum_{j_{1,2}, \dots, j_{L,2}=0}^{\infty} \prod_{\iota=1}^L \prod_{\ell=1}^2 \frac{K_{\iota,\ell}^{j_{\iota,\ell}} d_{\iota,\ell}^{j_{\iota,\ell}} m_{\iota,\ell}^{m_{\iota,\ell}}}{j_{\iota,\ell}! \Gamma(m_{\iota,\ell})} \frac{\gamma^2}{\Gamma(j_{\iota,\ell} + 1)} \frac{1}{2}$$

$$\times H_{2,0:3,2; \dots; 3,2,2,2}^{0,1:1,3; \dots; 1,3,2,1} \left(\begin{array}{c} \eta_1 \\ \vdots \\ \eta_L \\ \frac{1}{e} \end{array} \middle| \begin{array}{l} (1; -0.5, \dots, -0.5, -1), (0; 1, \dots, 1, 0) : v_{h_{FP},1}; \dots; v_{h_{FP},L}; (0, 1) \\ - : (0, 1), (-\gamma^2, 1); \dots; (0, 1), (-\gamma^2, 1); (0, 1), (0, 1); (1, 1) \end{array} \right), \quad (50)$$

where $\eta_{\varsigma} = A_0 \sqrt{e \frac{|h_L|^2 P}{N_o}} \prod_{\ell=1}^2 (\sqrt{2}\sigma_{\varsigma,\ell})$.

Proof: Please refer to Appendix D. ■

Proposition 3. *The effective capacity of the RIS-aid system for the case of ideal RF chains can be bounded by*

$$C_I \leq \log_2 \left(1 + \frac{P|h_L|^2 \mathbb{E} [|h_{FP}|^2]}{N_o} \right). \quad (51)$$

Proof: With the help of Jensen's inequality [36], the ergodic capacity can be upper-bounded as

$$C_I \leq \log_2 (1 + \mathbb{E} [\gamma_I]). \quad (52)$$

Substituting (43) into (52), we obtain (51) to complete the proof. ■

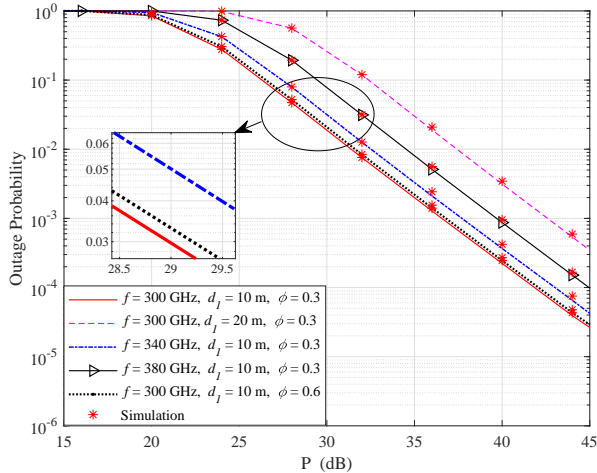


Fig. 8. Outage probability versus the transmit power with $d_2 = 20$ m, $N_0 = 1$ dB, $L = 40$, $m_{\ell,1} = 5$, $m_{\ell,2} = 7$, $K_{\ell,1} = 5$, $K_{\ell,2} = 6$, $\Delta_{\ell,1} = 0.6$, $\Delta_{\ell,2} = 0.4$, $\kappa_S = \kappa_D = 0.1$, and $2\sigma_{\ell,1}(1 + K_{\ell,1}) = 2\sigma_{\ell,2}(1 + K_{\ell,2}) = 20$ dB.

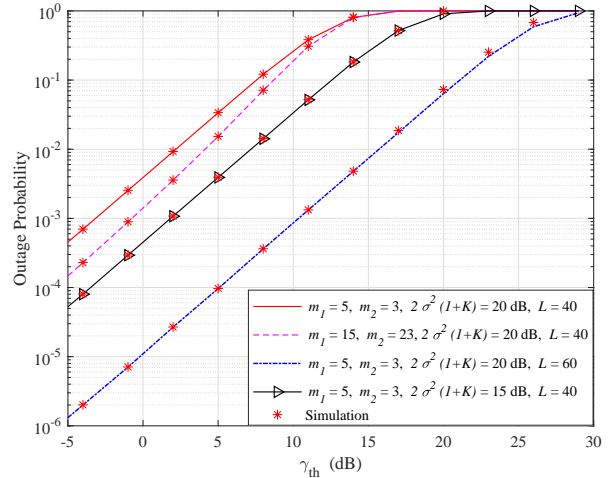


Fig. 9. OP versus the threshold, γ_{th} , with $P = 40$ dB, $m_{\ell,1} = m_1$, $m_{\ell,2} = m_2$, $2\sigma_{\ell,1}(1 + K_{\ell,1}) = 2\sigma_{\ell,2}(1 + K_{\ell,2}) = 2\sigma(1 + K)$, $f = 300$ GHz, $d_1 = 10$ m, $d_2 = 10$ m, $N_0 = 1$ dB, $K_{\ell,1} = 5$, $K_{\ell,2} = 6$, $\Delta_{\ell,1} = 0.6$, $\Delta_{\ell,2} = 0.4$, and $\kappa_S = \kappa_D = 0.1$.

From (48), (50), and (51), as expected, we can observe that the multipath parameters m have a positive effect to the ergodic capacity of RIS-aid THz communications.

VI. NUMERICAL RESULTS AND DISCUSSIONS

In this section, we present numerical results to investigate the joint impacts of misalignment, multipath fading, channel conditions, and transceivers hardware imperfections on the outage and ergodic capacity performance of the RIS-aided THz communications. Following the parameters in [7], we assume that $T = 27$ °C, $p = 101325$ Pa, $c = 3 \times 10^8$ m/s, $w_d/a = 6$, $G_t = G_r = 40$ dB, and $\sigma_S = 0.01$ m.

Figure 8 illustrates the OP performance versus the transmit power with $d_2 = 20$ m, $N_0 = 0$ dB, $L = 40$, $m_{\ell,1} = 5$, $m_{\ell,2} = 7$, $K_{\ell,1} = 5$, $K_{\ell,2} = 6$, $\Delta_{\ell,1} = 0.6$, $\Delta_{\ell,2} = 0.4$, $\kappa_S = \kappa_D = 0.1$, and $2\sigma_{\ell,1}(1 + K_{\ell,1}) = 2\sigma_{\ell,2}(1 + K_{\ell,2}) = 20$ dB ($\ell = 1, \dots, L$). For a given transmission distance, we can observe that the OP increases as the relative humidity increases. Furthermore, the increase in the transmission distance of the signal can cause a significant increase in the OP. Comparing the impact of the propagation loss and the molecular absorption loss, we can find an interesting insight is that the propagation loss is more detrimental to the performance of the RIS-aided THz communication system than the molecular absorption loss. This is because the OP degradation caused by the increase of d_1 is severer than the corresponding degradation caused by the increase of ϕ_1 . Moreover, as it can be observed, the outage probability increases as the frequency increases. When the frequency increases from 340 GHz

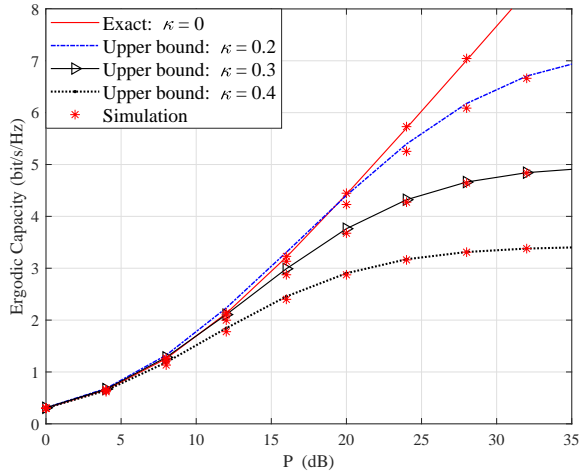


Fig. 10. Ergodic capacity versus the transmit power with $m_{\ell,1} = 5$, $m_{\ell,2} = 7$, $f = 360$ GHz, $d_1 = 8$ m, $d_2 = 6$ m, $N_0 = 1$ dB, $K_{\ell,1} = 5$, $K_{\ell,2} = 6$, $\Delta_{\ell,1} = 0.6$, $\Delta_{\ell,2} = 0.4$, $L = 40$, and $2\sigma_{\ell,1}(1 + K_{\ell,1}) = 2\sigma_{\ell,2}(1 + K_{\ell,2}) = 25$ dB ($\ell = 1, \dots, L$).

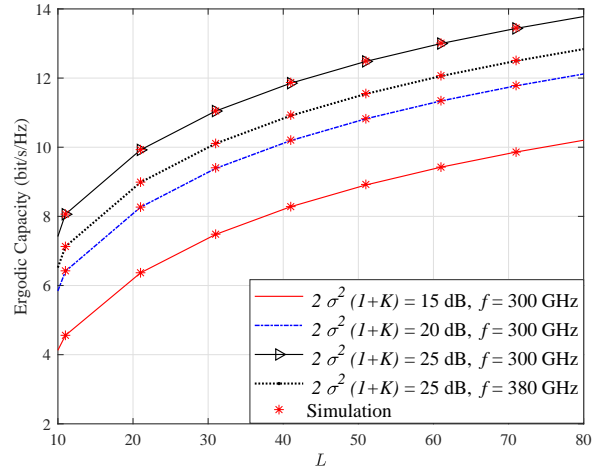


Fig. 11. Ergodic capacity versus the number of RIS's reflecting elements with $\kappa_S = \kappa_D = 0$, $m_{\ell,1} = 5$, $m_{\ell,2} = 7$, $d_1 = 8$ m, $d_2 = 6$ m, $N_0 = 1$ dB, $K_{\ell,1} = 5$, $K_{\ell,2} = 6$, $\Delta_{\ell,1} = 0.6$, and $\Delta_{\ell,2} = 0.4$.

to 380 GHz, the OP decreases faster than when the frequency increases from 300 GHz to 340 GHz. The reason is that a high molecular absorption exists in 380 GHz because 380 GHz is one of the water vapor resonance frequencies [37]. Thus, taking into account the variation of the environmental conditions and the molecular absorption phenomenon is significant for the THz communication system designer.

Figure 9 plots the OP versus the threshold, γ_{th} , with $P = 40$ dB, $m_{\ell,1} = m_1$, $m_{\ell,2} = m_2$, $2\sigma_{\ell,1}(1 + K_{\ell,1}) = 2\sigma_{\ell,2}(1 + K_{\ell,2}) = 2\sigma(1 + K)$, $f = 300$ GHz, $d_1 = 10$ m, $d_2 = 20$ m, $N_0 = 1$ dB, $K_{\ell,1} = 5$, $K_{\ell,2} = 6$, $\Delta_{\ell,1} = 0.6$, $\Delta_{\ell,2} = 0.4$, and $\kappa_S = \kappa_D = 0.1$. Obviously, as the increase of γ_{th} , the OP increase. Moreover, Fig. 9 shows the effects of different channel conditions. The OP decreases as shaping parameters m_1 and m_2 increasing because of the better channel conditions. Furthermore, the number of RIS's reflecting elements, L , has a significant impact on the performance of the RIS-aided THz communications. This is because that the RIS can effectively change the phase of reflected signals to enhance the received signal quality, enabling the desired THz wireless channel to exhibit a perfect line-of-sight.

Figure 10 depicts the ergodic capacity versus the transmit power with $m_{\ell,1} = 5$, $m_{\ell,2} = 7$, $f = 360$ GHz, $d_1 = 8$ m, $d_2 = 6$ m, $N_0 = 1$ dB, $K_{\ell,1} = 5$, $K_{\ell,2} = 6$, $\Delta_{\ell,1} = 0.6$, $\Delta_{\ell,2} = 0.4$, $L = 40$, and $2\sigma_{\ell,1}(1 + K_{\ell,1}) = 2\sigma_{\ell,2}(1 + K_{\ell,2}) = 25$ ($\ell = 1, \dots, L$) for different $\kappa_S = \kappa_D = \kappa$. We can observe the ergodic capacity increases when the transmission power increases. Thus, increasing the transmission power can be regarded as a direct measure to reduce the impact of hardware imperfections. Furthermore, Fig 10 reveals that the hardware imperfections have a small effect on the ergodic capacity in the low

transmit power regime, but their impact is detrimental in the high transmit power regime. Therefore, the efficient method to increase the ergodic capacity is to decrease the hardware imperfections when the transmit power is high. In addition, we can observe that the derived capacity upper bound is close to the Monte Carlo simulation results.

Figure 11 illustrates the ergodic capacity versus the number of RIS's reflecting elements with $2\sigma_{\ell,1}(1 + K_{\ell,1}) = 2\sigma_{\ell,2}(1 + K_{\ell,2}) = 2\sigma(1 + K)$, $\kappa_S = \kappa_D = 0$, $m_{\ell,1} = 5$, $m_{\ell,2} = 7$, $d_1 = 8$ m, $d_2 = 6$ m, $N_0 = 1$ dB, $K_{\ell,1} = 5$, $K_{\ell,2} = 6$, $\Delta_{\ell,1} = 0.6$, and $\Delta_{\ell,2} = 0.4$ for different f and $2\sigma(1 + K)$. From Fig. 11, we can observe that the ergodic capacity increases as the increase of number of reflecting elements. This is due to the reason that more elements let RIS has superior capability in manipulating electromagnetic waves. Thus, Equipping RIS with more reflecting elements can significantly improving the performance of wireless communication system. Furthermore, as it can be observed, the ergodic capacity decrease when the operation frequency is changed from 300 GHz to 380 GHz. Thus, it becomes evident that the system's performance will be significantly influenced by the selection of operation frequency, which also verify the conclusion obtained from Fig. 8.

VII. CONCLUSIONS

We investigate a RIS-aided THz communication system and provide a comprehensive analytical framework. Exact expressions of the end-to-end SNR and SNDR are presented. Furthermore, based on the measurement data, we prove that the FTR distribution performs a good fit for modeling the small-scale amplitude fading of THz signals. A method of the phase-shifts design at the RIS elements under discrete phase-shifts constraints was proposed. Moreover, we investigate the impact of different number of discrete phase-shifts levels. Furthermore, important performance metrics, including the OP and ergodic capacity, are derived with closed-form expressions in terms of the multivariate Fox's H -function. The tight upper bound expressions of ergodic capacity for ideal and non-ideal RF chains are also obtained. Finally, numerical results confirm that the propagation loss is more detrimental to the performance of the RIS-aided THz communication system than the molecular absorption loss, and the RIS can bring significant performance gain for the proposed THz communications.

APPENDIX A

PROOF OF LEMMA 1

A. Proof of PDF

With the help of (36), γ_N can be expressed as

$$\gamma_N = \frac{|h_L|^2 P}{N_o} \frac{1}{\frac{\kappa^2 |h_L|^2 P}{N_o} + \frac{1}{|h_{FP}|^2}}. \quad (\text{A-1})$$

Thus, we obtain

$$\frac{1}{\gamma_N} = \kappa^2 + \frac{N_o}{|h_L|^2 P} \frac{1}{|h_{FP}|^2}. \quad (\text{A-2})$$

Let us define that $V = \frac{1}{|h_{FP}|^2}$, $W = \frac{N_o}{|h_L|^2 P} V = \frac{1}{\gamma_N} - \kappa^2$. The PDF of V and W can be respectively expressed as

$$f_V(v) = -\frac{1}{2v^2 \sqrt{\frac{1}{v}}} f_{|h_{FP}|} \left(\sqrt{\frac{1}{v}} \right), \quad (\text{A-3})$$

$$f_W(w) = \frac{|h_L|^2 P}{N_o} f_V \left(\frac{|h_L|^2 P}{N_o} w \right). \quad (\text{A-4})$$

Substituting (A-3) into (A-4), we obtain

$$f_W(w) = \frac{-1}{2w^2 \sqrt{\frac{|h_L|^2 P}{N_o w}}} f_{|h_{FP}|} \left(\sqrt{\frac{N_o}{|h_L|^2 P w}} \right). \quad (\text{A-5})$$

By performing the change of variables $\gamma_N = \frac{1}{W + \kappa^2}$, f_{γ_N} can be rewritten as

$$f_{\gamma_N}(x) = \frac{1}{x^2} \frac{1}{2 \left(\frac{1-x\kappa^2}{x} \right)^2} \frac{1}{\sqrt{\frac{|h_L|^2 P}{N_o \frac{1-x\kappa^2}{x}}}} f_{|h_{FP}|} \left(\sqrt{\frac{N_o}{|h_L|^2 P \frac{1-x\kappa^2}{x}}} \right). \quad (\text{A-6})$$

Moreover, with the help of [38, eq. (62)], we obtain the PDF of $|h_{FP}|$ as

$$f_{|h_{FP}|}(x) = \int_0^{A_o} \frac{1}{y} f_{|h_F|} \left(\frac{x}{y} \right) f_{|h_P|}(y) dy. \quad (\text{A-7})$$

Substituting (A-7) into (A-6), we derive the integral representation for the PDF of $|h_{FP}|$ as (37) to complete the proof.

B. Proof of CDF

Following similar procedures as Appendix A-A, we can derive the CDF of V and W as

$$F_V(v) = F_{|h_{FP}|} \left(\sqrt{\frac{1}{v}} \right), \quad (\text{A-8})$$

$$F_W(w) = F_V \left(\frac{|h_L|^2 P}{N_o} w \right). \quad (\text{A-9})$$

Making the change of variable $\gamma_N = \frac{1}{W + \kappa^2}$, we can derive the CDF of γ_N as

$$F_{\gamma_N}(x) = F_{|h_{FP}|} \left(\sqrt{\frac{x N_o}{|h_L|^2 P (1 - x \kappa^2)}} \right). \quad (\text{A-10})$$

With the help of [38, eq. (65)], the CDF of $|h_{FP}|$ can be expressed as

$$F_{|h_{FP}|}(x) = \int_0^{A_o} F_{|h_F|} \left(\frac{x}{y} \right) f_{|h_F|}(y) dy. \quad (\text{A-11})$$

Substituting (A-11) into (A-10), the integral representation for the CDF of $|h_{FP}|$ as (38) can be derived to complete the proof.

APPENDIX B

PROOF OF THEOREM 1

A. Proof of PDF

With the help of the definition of multivariate Fox's H -function [30, eq. (A-1)], eq. (31) can be expressed as

$$\begin{aligned} f_{|h_F|}(y) = & \sum_{j_{1,1}, \dots, j_{L,1}=0}^{\infty} \sum_{j_{1,2}, \dots, j_{L,2}=0}^{\infty} \prod_{\ell=1}^L \prod_{i=1}^2 \frac{K_{\ell, \ell}^{j_{\ell, \ell}} d_{\ell, \ell}^{j_{\ell, \ell}} m_{\ell, \ell}^{m_{\ell, \ell}}}{j_{\ell, \ell}!} \frac{1}{\Gamma(m_{\ell, \ell}) \Gamma(j_{\ell, \ell} + 1)} \\ & \times \frac{1}{y} \prod_{i=1}^L \frac{1}{2\pi^i} \int_{\mathcal{L}_\ell} \frac{\prod_{\ell=1}^2 \Gamma(1 + j_{\ell, \ell} + \frac{1}{2} s_\ell) \Gamma(-s_\ell)}{\Gamma(-\sum_{\ell=1}^L s_\ell)} \left(y^{-1} \prod_{\ell=1}^2 (\sqrt{2} \sigma_{\ell, \ell}) \right)^{s_\ell} ds_\ell, \end{aligned} \quad (\text{B-1})$$

where the integration path of \mathcal{L}_ℓ ($\ell = 1, 2, \dots, L$) goes from $a_\ell - \infty j$ to $a_\ell + \infty j$ and $a_\ell \in \mathbb{R}$. Substituting (B-1) and (14) into (A-7), we obtain that

$$f_{|h_{FP}|}(x) = \int_0^{A_0} \frac{1}{y} \sum_{j_{1,1}, \dots, j_{L,1}=0}^{\infty} \cdots \sum_{j_{1,N}, \dots, j_{L,N}=0}^{\infty} \prod_{\iota=1}^L \prod_{\ell=1}^2 \frac{K_{\iota,\ell}^{j_{\iota,\ell}} d_{\iota,\ell} j_{\iota,\ell} m_{\iota,\ell}^{m_{\iota,\ell}}}{j_{\iota,\ell}!} \frac{1}{\Gamma(m_{\iota,\ell})} \frac{1}{\Gamma(j_{\iota,\ell} + 1)} \frac{y}{x} \\ \times \prod_{\iota=1}^L \frac{1}{2\pi i} \int_{\mathcal{L}_\ell} \frac{\prod_{\ell=1}^2 \Gamma(1 + j_{\iota,\ell} + \frac{1}{2}\varsigma_\ell) \Gamma(-\varsigma_\ell)}{\Gamma\left(-\sum_{\iota=1}^L \varsigma_\ell\right)} \left(\frac{y}{x} \prod_{\ell=1}^2 (\sqrt{2}\sigma_{\iota,\ell})\right)^{\varsigma_\ell} d\varsigma_\ell \frac{\gamma^2}{A_0^{\gamma^2}} x^{\gamma^2-1} dy. \quad (\text{B-2})$$

With the help of Fubini's theorem, the order of integrations in (B-2) can be exchanged. Thus, We obtain

$$f_{|h_{FP}|}(x) = \sum_{j_{1,1}, \dots, j_{L,1}=0}^{\infty} \cdots \sum_{j_{1,N}, \dots, j_{L,N}=0}^{\infty} \prod_{\iota=1}^L \prod_{\ell=1}^2 \frac{K_{\iota,\ell}^{j_{\iota,\ell}} d_{\iota,\ell} j_{\iota,\ell} m_{\iota,\ell}^{m_{\iota,\ell}}}{j_{\iota,\ell}!} \frac{1}{\Gamma(m_{\iota,\ell})} \frac{1}{\Gamma(j_{\iota,\ell} + 1)} \frac{\gamma^2}{xA_0^{\gamma^2}} \\ \times \prod_{\iota=1}^L \frac{1}{2\pi i} \int_{\mathcal{L}_\ell} \frac{\prod_{\ell=1}^2 \Gamma(1 + j_{\iota,\ell} + \frac{1}{2}\varsigma_\ell) \Gamma(-\varsigma_\ell)}{\Gamma\left(-\sum_{\iota=1}^L \varsigma_\ell\right)} \left((x)^{-1} \prod_{\ell=1}^2 (\sqrt{2}\sigma_{\iota,\ell})\right)^{\varsigma_\ell} I_A d\varsigma_\ell, \quad (\text{B-3})$$

where

$$I_A = \int_0^{A_0} y^{\varsigma_\ell + \gamma^2 - 1} dy = \frac{1}{\varsigma_\ell + \gamma^2} A_0^{\varsigma_\ell + \gamma^2}. \quad (\text{B-4})$$

With the aid of [26, eq. (8.331.1)], I_A can be expressed as

$$I_A = \frac{\Gamma(\varsigma_\ell + \gamma^2)}{\Gamma(\varsigma_\ell + \gamma^2 + 1)} A_0^{\varsigma_\ell + \gamma^2}. \quad (\text{B-5})$$

Substituting I_A into (B-3) and using the definition of multivariate Fox's H -function [30, eq. (A-1)], we obtain (39) that completes the proof.

B. Proof of CDF

Using [30, eq. (A-1)], we can rewrite (32) as

$$F_{|h_F|}(y) = \sum_{j_{1,1}, \dots, j_{L,1}=0}^{\infty} \sum_{j_{1,2}, \dots, j_{L,2}=0}^{\infty} \prod_{\iota=1}^L \prod_{\ell=1}^2 \frac{K_{\iota,\ell}^{j_{\iota,\ell}} d_{\iota,\ell} j_{\iota,\ell} m_{\iota,\ell}^{m_{\iota,\ell}}}{j_{\iota,\ell}!} \frac{1}{\Gamma(m_{\iota,\ell})} \frac{1}{\Gamma(j_{\iota,\ell} + 1)} \\ \times \prod_{\iota=1}^L \frac{1}{2\pi i} \int_{\mathcal{L}_\ell} \frac{\prod_{\ell=1}^2 \Gamma(1 + j_{\iota,\ell} + \frac{1}{2}\varsigma_\ell) \Gamma(-\varsigma_\ell)}{\Gamma\left(1 - \sum_{\iota=1}^L \varsigma_\ell\right)} \left(y^{-1} \prod_{\ell=1}^2 (\sqrt{2}\sigma_{\iota,\ell})\right)^{\varsigma_\ell} d\varsigma_\ell. \quad (\text{B-6})$$

Substituting (B-6) and (14) into (A-11), we can express the CDF of $|h_{FP}|$ as

$$F_{|h_{FP}|}(x) = \int_0^{A_o} \sum_{j_{1,1}, \dots, j_{L,1}=0}^{\infty} \cdots \sum_{j_{1,N}, \dots, j_{L,N}=0}^{\infty} \prod_{\ell=1}^L \prod_{i=1}^2 \frac{K_{\ell, \ell}^{j_{\ell, \ell}} d_{\ell, \ell}^{j_{\ell, \ell}} m_{\ell, \ell}^{m_{\ell, \ell}}}{j_{\ell, \ell}!} \frac{1}{\Gamma(m_{\ell, \ell}) \Gamma(j_{\ell, \ell} + 1)} \\ \times \prod_{i=1}^L \frac{1}{2\pi i} \int_{\mathcal{L}_i} \frac{\prod_{\ell=1}^2 \Gamma(1 + j_{\ell, \ell} + \frac{1}{2}\varsigma_{\ell}) \Gamma(-\varsigma_{\ell})}{\Gamma\left(1 - \sum_{\ell=1}^L \varsigma_{\ell}\right)} \left(\frac{y}{x} \prod_{\ell=1}^2 (\sqrt{2}\sigma_{\ell, \ell})\right)^{\varsigma_{\ell}} d\varsigma_{\ell} \frac{\gamma^2}{A_o^{\gamma^2}} y^{\gamma^2-1} dy. \quad (\text{B-7})$$

According to Fubini's theorem, we notice that the order of integration can be interchangeable, and can rewrite (B-7) as

$$F_{|h_{FP}|}(x) = \sum_{j_{1,1}, \dots, j_{L,1}=0}^{\infty} \cdots \sum_{j_{1,N}, \dots, j_{L,N}=0}^{\infty} \prod_{\ell=1}^L \prod_{i=1}^2 \frac{K_{\ell, \ell}^{j_{\ell, \ell}} d_{\ell, \ell}^{j_{\ell, \ell}} m_{\ell, \ell}^{m_{\ell, \ell}}}{j_{\ell, \ell}!} \frac{1}{\Gamma(m_{\ell, \ell}) \Gamma(j_{\ell, \ell} + 1)} \frac{\gamma^2}{A_o^{\gamma^2}} \\ \times \prod_{i=1}^L \frac{1}{2\pi i} \int_{\mathcal{L}_i} \frac{\prod_{\ell=1}^2 \Gamma(1 + j_{\ell, \ell} + \frac{1}{2}\varsigma_{\ell}) \Gamma(-\varsigma_{\ell})}{\Gamma\left(1 - \sum_{\ell=1}^L \varsigma_{\ell}\right)} \left(\frac{1}{x} \prod_{\ell=1}^2 (\sqrt{2}\sigma_{\ell, \ell})\right)^{\varsigma_{\ell}} I_A d\varsigma_{\ell}, \quad (\text{B-8})$$

where I_A has been solved as (B-5). Substituting I_A into (B-8), the CDF of $|h_{FP}|$ can be expressed as eq. (40) that completes the proof.

APPENDIX C

PROOF OF PROPOSITION 1

With the help of Jensen's inequality [36], the upper-bound of the ergodic capacity can be expressed as

$$C_N \leq \log_2(1 + \mathbb{E}[\gamma_N]), \quad (\text{C-1})$$

where

$$\mathbb{E}[\gamma_N] = \mathbb{E}\left[\frac{|h_{FP}|^2 |h_L|^2 P}{\kappa^2 |h_{FP}|^2 |h_L|^2 P + N_o}\right] = \frac{P |h_L|^2 \mathbb{E}[|h_{FP}|^2]}{P \kappa^2 |h_L|^2 \mathbb{E}[|h_{FP}|^2] + N_o}. \quad (\text{C-2})$$

The s_{th} moment of $|h_{FP}|$ is defined as

$$\mathbb{E}[|h_{FP}|^s] = \int_0^{\infty} x^s f_{h_{FP}}(x) dx. \quad (\text{C-3})$$

Substituting (39) into (C-3), $\mathbb{E}[|h_{FP}|^s]$ can be expressed as

$$\begin{aligned} \mathbb{E}[|h_{FP}|^s] = & \sum_{j_{1,1}, \dots, j_{L,1}=0}^{\infty} \cdots \sum_{j_{1,N}, \dots, j_{L,N}=0}^{\infty} \prod_{\iota=1}^L \prod_{\ell=1}^2 \frac{K_{\iota,\ell}^{j_{\iota,\ell}} d_{\iota,\ell} j_{\iota,\ell} m_{\iota,\ell}^{m_{\iota,\ell}} \gamma^2}{j_{\iota,\ell}! \Gamma(m_{\iota,\ell}) \Gamma(j_{\iota,\ell} + 1)} \\ & \times \prod_{\iota=1}^L \frac{1}{2\pi i} \int_{\mathcal{L}_\ell} \frac{\prod_{\ell=1}^2 \Gamma(1 + j_{\iota,\ell} + \frac{1}{2} \varsigma_\ell) \Gamma(-\varsigma_\ell) \Gamma(\varsigma_\ell + \gamma^2)}{\Gamma(-\sum_{\iota=1}^L \varsigma_\ell) \Gamma(\varsigma_\ell + \gamma^2 + 1)} \left(A_0 \prod_{\ell=1}^2 (\sqrt{2} \sigma_{\iota,\ell}) \right)^{\varsigma_\ell} I_C d\varsigma_\ell, \end{aligned} \quad (\text{C-4})$$

where

$$I_C = \int_0^\infty x^{s - \sum_{\iota=1}^L \varsigma_\iota - 1} dx. \quad (\text{C-5})$$

Let $\mathcal{L}\{p(t)\} = P(x)$. With the help of the property of Laplace transform, it follows that

$$\mathcal{L}\left\{ \int_0^t p(z) dz \right\} = \frac{P(x)}{x}. \quad (\text{C-6})$$

According to the final value theorem, we have

$$\lim_{t \rightarrow \infty} \left(\int_0^t p(z) dz \right) = e \frac{P(e)}{e} = P(e), \quad (\text{C-7})$$

where e is a number close to zero (e.g., $e = 10^{-6}$). Thus, we can use (C-7) to solve I_C as

$$I_C = \left(\frac{1}{e} \right)^{s - \sum_{\iota=1}^L \varsigma_\iota} \Gamma\left(s - \sum_{\iota=1}^L \varsigma_\iota \right). \quad (\text{C-8})$$

Substituting (C-8) into (C-4) and using the definition of multivariate Fox's H -function [30, eq. (A-1)], we obtain

$$\begin{aligned} \mathbb{E}[|h_{FP}|^s] = & \sum_{j_{1,1}, \dots, j_{L,1}=0}^{\infty} \sum_{j_{1,2}, \dots, j_{L,2}=0}^{\infty} \prod_{\iota=1}^L \prod_{\ell=1}^2 \frac{K_{\iota,\ell}^{j_{\iota,\ell}} d_{\iota,\ell} j_{\iota,\ell} m_{\iota,\ell}^{m_{\iota,\ell}} \gamma^2}{j_{\iota,\ell}! \Gamma(m_{\iota,\ell}) \Gamma(j_{\iota,\ell} + 1)} \left(\frac{1}{e} \right)^s \\ & \times H_{2,0:3,2; \dots; 3,2}^{0,1:1,3; \dots; 1,3} \left(\begin{array}{c} e A_0 \prod_{\ell=1}^2 (\sqrt{2} \sigma_{1,\ell}) \\ \vdots \\ e A_0 \prod_{\ell=1}^2 (\sqrt{2} \sigma_{L,\ell}) \end{array} \middle| \begin{array}{c} (1-s; -1, \dots, -1), (0; -1, \dots, -1) : \nu_{FP,1}; \dots; \nu_{FP,L} \\ - : (0, 1), (-\gamma^2, 1); \dots; (0, 1), (-\gamma^2, 1) \end{array} \right). \end{aligned} \quad (\text{C-9})$$

Combining (C-9) and (C-2), letting $s = 2$, we obtain (48) to complete the proof.

APPENDIX D

PROOF OF PROPOSITION 2

for the case of ideal RF chains, the ergodic capacity can be expressed as

$$C_I = E[\log_2(1 + \gamma_I)] = \int_0^\infty \log_2(1 + x) f_{|\gamma_I|}(x) dx. \quad (\text{D-1})$$

Substituting (44) into (D-1), we obtain

$$C_I = \frac{1}{2} \sum_{j_{1,1}, \dots, j_{L,1}=0}^\infty \sum_{j_{1,2}, \dots, j_{L,2}=0}^\infty \prod_{\iota=1}^L \prod_{\ell=1}^2 \frac{K_{\iota,\ell}^{j_{\iota,\ell}} d_{\iota,\ell}^{j_{\iota,\ell}} m_{\iota,\ell}^{m_{\iota,\ell}}}{j_{\iota,\ell}!} \frac{\gamma^2}{\Gamma(m_{\iota,\ell}) \Gamma(j_{\iota,\ell} + 1)} \\ \times \prod_{\iota=1}^L \frac{1}{2\pi i} \int_{\mathcal{L}_\ell} \frac{\prod_{\ell=1}^2 \Gamma(1 + j_{\iota,\ell} + \frac{1}{2}s_\ell) \Gamma(-s_\ell) \Gamma(s_\ell + \gamma^2)}{\Gamma\left(-\sum_{\iota=1}^L s_\ell\right) \Gamma(s_\ell + \gamma^2 + 1)} \left(A_0 \sqrt{\frac{|h_L|^2 P}{N_o}} \prod_{\ell=1}^2 \left(\sqrt{2}\sigma_{\iota,\ell} \right) \right)^{s_\ell} I_{D_1} d s_\ell, \quad (\text{D-2})$$

where

$$I_{D_1} = \int_0^\infty \log_2(1 + x) x^{-1 - \frac{1}{2} \sum_{\iota=1}^L s_\ell} dx. \quad (\text{D-3})$$

With the aid of [39, eq. (01.04.07.0002.01)], I_{D_1} can be expressed as

$$I_{D_1} = \frac{1}{2\pi i} \int_{\mathcal{L}_{L+1}} \frac{\Gamma(s_{L+1} + 1) \Gamma^2(-s_{L+1})}{\Gamma(1 - s_{L+1})} I_{D_2} d s_{L+1}, \quad (\text{D-4})$$

where I_{D_2} can be solved by following similar procedures as (C-7) as

$$I_{D_2} = \int_0^\infty x^{-1 - \frac{1}{2} \sum_{\iota=1}^L s_\ell - s_{L+1}} dx = \left(\frac{1}{e} \right)^{-\frac{1}{2} \sum_{\iota=1}^L s_\ell - s_{L+1}} \Gamma\left(-\frac{1}{2} \sum_{\iota=1}^L s_\ell - s_{L+1} \right). \quad (\text{D-5})$$

Substituting (D-5) and (D-4) into (D-2), we obtain

$$C_I = \sum_{j_{1,1}, \dots, j_{L,1}=0}^\infty \sum_{j_{1,2}, \dots, j_{L,2}=0}^\infty \prod_{\iota=1}^L \prod_{\ell=1}^2 \frac{K_{\iota,\ell}^{j_{\iota,\ell}} d_{\iota,\ell}^{j_{\iota,\ell}} m_{\iota,\ell}^{m_{\iota,\ell}}}{j_{\iota,\ell}!} \frac{\gamma^2}{\Gamma(m_{\iota,\ell}) \Gamma(j_{\iota,\ell} + 1)} \frac{1}{2} \\ \times \prod_{\iota=1}^L \frac{1}{2\pi i} \int_{\mathcal{L}_\ell} \frac{\prod_{\ell=1}^2 \Gamma(1 + j_{\iota,\ell} + \frac{1}{2}s_\ell) \Gamma(-s_\ell) \Gamma(s_\ell + \gamma^2)}{\Gamma\left(-\sum_{\iota=1}^L s_\ell\right) \Gamma(s_\ell + \gamma^2 + 1)} \left(A_0 \sqrt{e \frac{|h_L|^2 P}{N_o}} \prod_{\ell=1}^2 \left(\sqrt{2}\sigma_{\iota,\ell} \right) \right)^{s_\ell} \\ \times \frac{1}{2\pi i} \int_{\mathcal{L}_{L+1}} \frac{\Gamma(s_{L+1} + 1) \Gamma^2(-s_{L+1}) \Gamma\left(-\frac{1}{2} \sum_{\iota=1}^L s_\ell - s_{L+1}\right)}{\Gamma(1 - s_{L+1})} e^{-s_{L+1}} d s_{L+1} d s_\ell. \quad (\text{D-6})$$

With the help of [30, eq. (A-1)], we can rewrite (D-6) as (50) that completes the proof.

REFERENCES

- [1] M. Agiwal, A. Roy, and N. Saxena, "Next generation 5G wireless networks: A comprehensive survey," *IEEE Commun. Surveys Tuts.*, vol. 18, no. 3, pp. 1617–1655, 3rd Quart. 2016.
- [2] A.-A. A. Boulogeorgos, A. Alexiou, and T. Merkle, "Terahertz technologies to deliver optical network quality of experience in wireless systems beyond 5G," *IEEE Commun. Mag.*, vol. 56, no. 6, pp. 144–151, Jun. 2018.
- [3] A.-A. A. Boulogeorgos, S. K. Goudos, and A. Alexiou, "Users association in ultra dense THz networks," in *Proc. IEEE Int. Workshop Signal Process. Adv. Wireless Commun. (SPAWC)*. IEEE, Jun. 2018, pp. 1–5.
- [4] E. Basar, M. Di Renzo, J. De Rosny, M. Debbah, M.-S. Alouini, and R. Zhang, "Wireless communications through reconfigurable intelligent surfaces," *IEEE Access*, vol. 7, pp. 116 753–116 773, Aug. 2019.
- [5] C. Huang, A. Zappone, G. C. Alexandropoulos, M. Debbah, and C. Yuen, "Reconfigurable intelligent surfaces for energy efficiency in wireless communication," *IEEE Trans. Wireless Commun.*, vol. 18, no. 8, pp. 4157–4170, Aug. 2019.
- [6] Y. Han, W. Tang, S. Jin, C.-K. Wen, and X. Ma, "Large intelligent surface-assisted wireless communication exploiting statistical CSI," *IEEE Trans. Veh. Technol.*, vol. 68, no. 8, pp. 8238–8242, Aug. 2019.
- [7] J. Kokkonen, J. Lehtomaki, and M. Juntti, "Simplified molecular absorption loss model for 275-400 gigahertz frequency band," in *Proc. 12th Eur. Conf. Antennas Propag. (EuCAP)*, Apr. 2018, pp. 1–5.
- [8] A.-A. A. Boulogeorgos, E. N. Papatotiriou, J. Kokkonen, J. Lehtomaki, A. Alexiou, and M. Juntti, "Performance evaluation of THz wireless systems operating in 275-400 GHz band," in *Proc. IEEE Veh. Technol. Conf. (VTC)*. IEEE, Jun. 2018, pp. 1–5.
- [9] A. R. Ekti, A. Boyaci, A. Alparslan, İ. Ünal, S. Yarkan, A. Görçin, H. Arslan, and M. Uysal, "Statistical modeling of propagation channels for terahertz band," in *Proc. IEEE Conf. Standards Commun. Netw. (CSCN)*. IEEE, Sept. 2017, pp. 275–280.
- [10] S. Priebe, C. Jastrow, M. Jacob, T. Kleine-Ostmann, T. Schrader, and T. Kurner, "Channel and propagation measurements at 300 GHz," *IEEE Trans. Antennas Propag.*, vol. 59, no. 5, pp. 1688–1698, May 2011.
- [11] K. Guan, B. Peng, D. He, J. M. Eckhardt, S. Rey, B. Ai, Z. Zhong, and T. Kürner, "Measurement, simulation, and characterization of train-to-infrastructure inside-station channel at the terahertz band," *IEEE Trans. THz Sci. Technol.*, vol. 9, no. 3, pp. 291–306, Mar. 2019.
- [12] J. M. Romero-Jerez, F. J. Lopez-Martinez, J. F. Paris, and A. J. Goldsmith, "The fluctuating two-ray fading model: Statistical characterization and performance analysis," *IEEE Trans. Wireless Commun.*, vol. 16, no. 7, pp. 4420–4432, Jul. 2017.
- [13] J. Zhang, H. Du, P. Zhang, J. Cheng, and L. Yang, "Performance analysis of 5G mobile relay systems for high-speed trains," *IEEE J. Select. Areas Commun.*, to appear, 2020.
- [14] Q. Wu and R. Zhang, "Intelligent reflecting surface enhanced wireless network via joint active and passive beamforming," *IEEE Trans. Wireless Commun.*, vol. 18, no. 11, pp. 5394–5409, Nov. 2019.
- [15] J. Oyedepo, Y. Salihu, and A. Folaponmile, "Interference mitigation techniques in wireless communications systems," *J. Research National Develop.*, vol. 8, no. 2, Feb 2010.
- [16] T. Schenk, *RF imperfections in high-rate wireless systems: Impact and digital compensation*. Springer Science & Business Media, 2008.
- [17] E. Björnson, M. Matthaiou, and M. Debbah, "A new look at dual-hop relaying: Performance limits with hardware impairments," *IEEE Trans. Commun.*, vol. 61, no. 11, pp. 4512–4525, Nov. 2013.
- [18] C. Studer, M. Wenk, and A. Burg, "MIMO transmission with residual transmit-RF impairments," in *Proc. Int. ITG Workshop Smart Antennas (WSA)*, Feb 2010, pp. 189–196.

- [19] D. Dardari, V. Tralli, and A. Vaccari, "A theoretical characterization of nonlinear distortion effects in OFDM systems," *IEEE Trans. Commun.*, vol. 48, no. 10, pp. 1755–1764, Oct. 2000.
- [20] B. E. Priyanto, T. B. Sorensen, O. K. Jensen, T. Larsen, T. Kolding, and P. Mogensen, "Assessing and modeling the effect of RF impairments on UTRA LTE uplink performance," in *Proc. IEEE Veh. Technol. Conf.*, Sept. 2007, pp. 1213–1217.
- [21] A.-A. A. Boulogeorgos, N. D. Chatzidiamantis, and G. K. Karagiannidis, "Energy detection spectrum sensing under RF imperfections," *IEEE Trans. Commun.*, vol. 64, no. 7, pp. 2754–2766, Jul. 2016.
- [22] T. L. Jensen and T. Larsen, "Robust computation of error vector magnitude for wireless standards," *IEEE Trans. Commun.*, vol. 61, no. 2, pp. 648–657, Feb. 2013.
- [23] T. J. Cui, S. Liu, and L. Zhang, "Information metamaterials and metasurfaces," *J. Mater. Chem. C*, vol. 5, no. 15, pp. 3644–3668, 2017.
- [24] J. M. Romero-Jerez, F. J. Lopez-Martinez, J. F. Paris, and A. J. Goldsmith, "The fluctuating two-ray fading model: Statistical characterization and performance analysis," *IEEE Trans. Wireless Commun.*, vol. 16, no. 7, pp. 4420–4432, Jul. 2017.
- [25] J. Zhang, W. Zeng, X. Li, Q. Sun, and K. P. Peppas, "New results on the fluctuating two-ray model with arbitrary fading parameters and its applications," *IEEE Trans. Veh. Technol.*, vol. 67, no. 3, pp. 2766–2770, Mar. 2017.
- [26] I. S. Gradshteyn and I. M. Ryzhik, *Table of Integrals, Series, and Products*, 7th ed. Academic Press, 2007.
- [27] A. A. Farid and S. Hranilovic, "Outage capacity optimization for free-space optical links with pointing errors," *IEEE/OSA J. Lightw. Technol.*, vol. 25, no. 7, pp. 1702–1710, Jul. 2007.
- [28] L. S. Rothman, I. E. Gordon, A. Barbe, D. C. Benner, P. F. Bernath, M. Birk, V. Boudon, L. R. Brown, A. Campargue, J.-P. Champion *et al.*, "The HITRAN 2008 molecular spectroscopic database," *J. Quant. Spectrosc. Radiat. Transf.*, vol. 110, no. 9-10, pp. 533–572, Jun. 2009.
- [29] H. Du, J. Zhang, J. Cheng, Z. Lu, and B. Ai, "Millimeter wave communications with reconfigurable intelligent surface: Performance analysis and optimization," *arXiv:2003.09090*, 2020.
- [30] A. M. Mathai, R. K. Saxena, and H. J. Haubold, *The H-function: Theory and Applications*. Springer Science & Business Media, 2009.
- [31] J. D. V. Sánchez, D. P. Moya Osorio, E. E. Benitez Olivo, H. Alves, M. C. Paredes Paredes, and L. Urquiza Aguiar, "On the statistics of the ratio of nonconstrained arbitrary α - μ random variables: A general framework and applications," *Trans. Emerging Tel. Tech.*, p. e3832, 2019.
- [32] C. R. N. Da Silva, N. Simmons, E. J. Leonardo, S. L. Cotton, and M. D. Yacoub, "Ratio of two envelopes taken from $\alpha - \mu$, $\eta - \mu$, and $\kappa - \mu$ variates and some practical applications," *IEEE Access*, vol. 7, pp. 54 449–54 463, May 2019.
- [33] H. R. Alhennawi, M. M. El Ayadi, M. H. Ismail, and H.-A. M. Mourad, "Closed-form exact and asymptotic expressions for the symbol error rate and capacity of the H -function fading channel," *IEEE Trans. Veh. Technol.*, vol. 65, no. 4, pp. 1957–1974, Apr. 2015.
- [34] H. Chergui, M. Benjillali, and M.-S. Alouini, "Rician K -factor-based analysis of XLOS service probability in 5G outdoor ultra-dense networks," *IEEE Wireless Commun. Lett.*, vol. 8, no. 2, pp. 428–431, Apr. 2018.
- [35] M.-S. Alouini and A. J. Goldsmith, "Capacity of Rayleigh fading channels under different adaptive transmission and diversity-combining techniques," *IEEE Trans. Veh. Technol.*, vol. 48, no. 4, pp. 1165–1181, Apr. 1999.
- [36] S. G. Krantz, *Handbook of complex variables*. Springer Science & Business Media, 2012.
- [37] C. Han, A. O. Bicen, and I. F. Akyildiz, "Multi-wideband waveform design for distance-adaptive wireless communications in the terahertz band," *IEEE Trans. Signal Process.*, vol. 64, no. 4, pp. 910–922, Feb. 2015.
- [38] A.-A. A. Boulogeorgos, E. N. Papasotiriou, and A. Alexiou, "Analytical performance assessment of THz wireless systems," *IEEE Access*, vol. 7, pp. 11 436–11 453, Feb. 2019.
- [39] Wolfram, "The wolfram functions site," <http://functions.wolfram.com>.